

Chapter 10

High-Order Flux Reconstruction Schemes

F.D. Witherden^{*}, P.E. Vincent[†] and A. Jameson^{*}

^{*}Stanford University, Stanford, CA, United States

[†]Imperial College London, South Kensington, London, United Kingdom

Chapter Outline

1 Introduction	228	5.1 Overview	244
2 FR in 1D	230	5.2 Salient Aspects of an FR Implementation	245
2.1 Advection Problems	230	6 Applications	246
2.2 Advection Diffusion	233	6.1 Solving the Euler and Navier–Stokes Equations	246
3 FR in Multidimensions	235	6.2 Flow Over a Circular Cylinder	247
3.1 Overview	235	6.3 Flow Over an SD7003 Wing	253
3.2 Tensor Product Elements	235	6.4 T106c Low-Pressure Turbine Cascade	255
3.3 Simplex Elements	236	7 Summary	258
4 Stability and Accuracy of FR Schemes	241	References	260
4.1 Energy Stability	241		
4.2 von Neumann Analysis	243		
4.3 Nonlinear Stability	243		
5 Implementation	244		

ABSTRACT

There is an increasing desire among industrial practitioners of computational fluid dynamics to undertake high-fidelity scale-resolving simulations of unsteady flows within the vicinity of complex geometries. Such simulations require numerical methods that can operate on unstructured meshes with low numerical dissipation. The flux reconstruction (FR) approach describes one such family of numerical methods, which includes a particular type of collocation-based nodal discontinuous Galerkin method, and spectral difference methods, as special cases. In this chapter we describe the current state-of-the-art surrounding research into FR methods. To begin, FR is described in one dimension for both advection and advection–diffusion problems. This is followed by a description of its extension to multidimensional tensor product and simplex elements. Stability and accuracy issues are then discussed, including an overview of energy-stability proofs, von Neumann analysis results, and stability characteristics when the flux function of the governing system is nonlinear. Finally, implementation aspects

are outlined in the context of modern hardware platforms, and three example applications of FR are presented, demonstrating the potential utility of FR schemes for scale resolving simulation of unsteady flow problems.

Keywords: High-order methods, Discontinuous Galerkin method, Flux reconstruction

AMS Classification Codes: 65M60, 65M70

1 INTRODUCTION

There is an increasing desire among industrial practitioners of computational fluid dynamics (CFD) to undertake high-fidelity scale-resolving simulations of transient compressible flows within the vicinity of complex geometries. For example, to improve the design of next generation aircraft, there exists a need to perform simulations—at Reynolds numbers 10^4 – 10^7 and Mach numbers $M \sim 0.1$ – 1.0 —of highly separated flow over deployed spoilers/air-brakes; separated flow within serpentine intake ducts and flow over entire vehicle configurations at off-design conditions. In order to perform these simulations it is necessary to solve the compressible Navier–Stokes equations. These take the form of a nonlinear conservation law.

When solving the Navier–Stokes equations numerically it is customary to independently discretise space and time. Although there exist a variety of spatial discretisations the three most popular are (Vincent and Jameson, 2011) the finite difference (FD) method in which the governing system is discretised onto a structured grid of points, the finite volume (FV) method in which the computational domain is decomposed into cells and an integral form of the governing system is solved within each cell, and the finite element (FE) method where the computational domain is decomposed into elements inside of which sits a polynomial that is required to satisfy a variational form of the governing system. All of these methods have been used successfully to solve fluid flow problems throughout both industry and academia.

An important consideration when choosing a discretisation is the order of accuracy. This dictates how the error in the solution will respond to a change in the resolution of the grid. Implementations of the above methods are usually first- or second-order accurate in space. A consequence of this is a large degree of numerical dissipation. Such schemes therefore encounter significant difficulties when attempting to simulate fundamentally unsteady phenomena (Jameson and Ou, 2011). This has led to an interest in high-order methods, the promise of which is increased accuracy with a decreased computational cost. One such example of a high-order spatial discretisation are classical spectral methods (Canuto et al., 2006). These methods involve decomposing the solution into modes (in frequency space), which are defined globally within the domain of interest. Spectral methods, however, typically lack the geometrical flexibility since it is often impossible to define continuous global modes within a complex geometry.

Alternatively, it is also possible to construct higher order formulations of the aforementioned FD, FV, and FE schemes. The order of accuracy of an FD scheme can be readily increased by simply expanding the size of the stencil. For FV methods the procedure is somewhat more involved. The most popular high-order FV type schemes are the essentially nonoscillatory (ENO) of Harten et al. (1987) and the weighted ENO (WENO) schemes of Liu et al. (1994). These schemes use an adaptive stencil through an unstructured grid in order to achieve a high-order reconstruction. The adaptive nature of the stencil allows both ENO and WENO schemes to automatically achieve high-order accuracy in the vicinity of shocks and other discontinuities. High-order FE schemes can be constructed by increasing the degree of the polynomial inside of each element. Such schemes are normally termed continuous Galerkin (CG) methods with elements being coupled by requiring that the approximate solution to be piecewise continuous between elements. Further details can be found in the books by Karniadakis and Sherwin (2005) and Solin et al. (2003). A popular alternative to CG is the discontinuous Galerkin (DG) finite element method, first introduced by Reed and Hill in 1973 to solve the neutron transport equation. In DG the solution is not required to be continuous between elements, instead coupling is achieved through the calculation of common fluxes at interfaces. This is similar to the coupling that occurs between cells in FV schemes.

Beyond CG and DG another more recent class of high-order schemes for unstructured grids are spectral difference (SD) methods. Originally proposed under the moniker ‘staggered-grid Chebyshev multidomain methods’ by Kopriva and Koliias in 1996 their use in CFD was popularised by Sun et al. (2007). In 2007 Huynh proposed the flux reconstruction (FR) approach; a unifying framework that encompasses both under integrated collocation-based nodal DG schemes and, at least for a linear flux function, any SD scheme. Following on from this, in 2009 Gao and Wang introduced a closely related set of methods which they referred to as lifting collocation penalty (LCP) schemes (Gao and Wang, 2009; Wang and Gao, 2009). Subsequently, in 2013 Yu and Wang showed in one dimension (1D) that the LCP schemes are identical to the FR approach. As such several authors have adopted the name corrections procedure via reconstruction (CPR) to refer to both FR and LCP. Furthermore, Allaneau and Jameson (2011) have showed that it is possible to cast some FR schemes as a filtered nodal DG scheme.

The remainder of this chapter is organised as follows. In Section 2 we present the FR approach in 1D for advection and advection–diffusion type hyperbolic conservation laws. Section 3 extends this methodology to quadrilaterals through a tensor product construction and simplex elements. The stability and accuracy of FR schemes are discussed in Section 4. It is shown how through the use of an energy method a family of one-parameter schemes can be obtained. Details surrounding the implementation of FR on modern

hardware platforms—including GPUs—are presented in [Section 5](#). In [Section 6](#) we show how FR can be used to solve the compressible Navier–Stokes equations in three dimensions and present results for a variety of benchmark flow problems. Finally, in [Section 7](#), conclusions are drawn.

2 FR IN 1D

2.1 Advection Problems

Consider using the FR approach to solve

$$\frac{\partial u}{\partial t} + \frac{\partial f}{\partial x} = 0 \quad (1)$$

within an arbitrary 1D domain Ω , where x is a spatial coordinate, t is time, $u = u(x, t)$ is a conserved scalar quantity, and $f = f(u)$ is the flux of u in the x direction.

The first stage of the FR approach involves partitioning Ω into N distinct elements, each denoted $\Omega_n = \{x | x_n < x < x_{n+1}\}$, such that

$$\Omega = \bigcup_{n=0}^{N-1} \Omega_n, \quad \bigcap_{n=0}^{N-1} \Omega_n = \emptyset. \quad (2)$$

The solution u in Eq. (1) is approximated in each Ω_n by $u_n^{\delta D} = u_n^{\delta D}(x, t)$, which is a polynomial of degree p within Ω_n , and the flux f in Eq. (1) is approximated in each Ω_n by $f_n^\delta = f_n^\delta(x, t)$, which is a polynomial of degree $p + 1$ within Ω_n . Consequently, a total approximate solution $u^{\delta D} = u^{\delta D}(x, t)$ and a total approximate flux $f^\delta = f^\delta(x, t)$ can be defined within Ω as

$$u^{\delta D} = \sum_{n=0}^{N-1} u_n^{\delta D} \approx u, \quad f^\delta = \sum_{n=0}^{N-1} f_n^\delta \approx f, \quad (3)$$

where no level of inter-element continuity in $u^{\delta D}$ is explicitly enforced. However, f^δ is required to be C_0 continuous at element interfaces.

The second stage of the FR approach involves transforming each Ω_n to a standard element $\Omega_S = \{\xi | -1 \leq \xi \leq 1\}$ via the mapping

$$\xi = \Gamma_n(x) = 2 \left(\frac{x - x_n}{x_{n+1} - x_n} \right) - 1, \quad (4)$$

which has the inverse

$$x = \Gamma_n^{-1}(\xi) = \left(\frac{1 - \xi}{2} \right) x_n + \left(\frac{1 + \xi}{2} \right) x_{n+1}. \quad (5)$$

Having performed such a transformation, the evolution of u_n^δ within any individual Ω_n (and thus the evolution of u^δ within Ω) can be determined by solving the following transformed equation within the standard element Ω_S

$$\frac{\partial \hat{u}^{\delta D}}{\partial t} + \frac{\partial \hat{f}^{\delta}}{\partial \xi} = 0, \quad (6)$$

where

$$\hat{u}^{\delta D} = \hat{u}^{\delta D}(\xi, t) = J_n u_n^{\delta D}(\Gamma_n^{-1}(\xi), t) \quad (7)$$

is a polynomial of degree p ,

$$\hat{f}^{\delta} = \hat{f}^{\delta}(\xi, t) = f_n^{\delta}(\Gamma_n^{-1}(\xi), t), \quad (8)$$

is a polynomial of degree $p + 1$, and $J_n = (x_{n+1} - x_n)/2$.

The third stage of the FR approach involves defining the degree p polynomial $\hat{u}^{\delta D}$ in terms of a nodal basis as follows

$$\hat{u}^{\delta D} = \sum_{i=0}^p \hat{u}_i^{\delta D} l_i, \quad (9)$$

where l_i are Lagrange polynomials defined as

$$l_i = \prod_{j=0, j \neq i}^p \left(\frac{\xi - \xi_j}{\xi_i - \xi_j} \right), \quad (10)$$

ξ_i ($i = 0$ to p) are $p + 1$ distinct solution points within Ω_S , and $\hat{u}_i^{\delta D} = \hat{u}_i^{\delta D}(t)$ ($i = 0$ to p) are values of $\hat{u}^{\delta D}$ at the solution points ξ_i .

The fourth stage of the FR approach involves constructing a degree p polynomial $\hat{f}^{\delta D} = \hat{f}^{\delta D}(\xi, t)$, defined as the approximate transformed discontinuous flux within Ω_S . Specifically, $\hat{f}^{\delta D}$ is obtained via a collocation projection at the $p + 1$ solution points, and can hence be expressed as

$$\hat{f}^{\delta D} = \sum_{i=0}^p \hat{f}_i^{\delta D} l_i, \quad (11)$$

where the coefficients $\hat{f}_i^{\delta D} = \hat{f}_i^{\delta D}(t)$ are simply values of the transformed flux at each solution point ξ_i (evaluated directly from the approximate solution). The flux $\hat{f}^{\delta D}$ is termed discontinuous since it is calculated directly from the approximate solution, which is in general discontinuous between elements.

The fifth stage of the FR approach involves evaluating $\hat{u}^{\delta D}$ at either end of the standard element Ω_S (i.e. at $\xi = \pm 1$). These values, in conjunction with analogous information from adjoining elements, are then used to calculate numerical interface fluxes. The exact methodology for calculating such numerical interface fluxes will depend on the nature of the equations being solved. For example, when solving the Euler equations one may use a Roe-type approximate Riemann solver (Roe, 1981), or any other two-point flux formula that provides for an upwind bias. In what follows the numerical

interface fluxes associated with the left- and right-hand ends of Ω_S (and transformed appropriately for use in Ω_S) will be denoted $\hat{f}_L^{\delta I}$ and $\hat{f}_R^{\delta I}$, respectively.

The penultimate stage of the FR approach involves constructing the degree $p + 1$ polynomial \hat{f}^{δ} , by adding a correction flux $\hat{f}^{\delta C} = \hat{f}^{\delta C}(\xi, t)$ of degree $p + 1$ to $\hat{f}^{\delta D}$, such that their sum equals the transformed numerical interface flux at $\xi = \pm 1$, yet in some sense follows $\hat{f}^{\delta D}$ within the interior of Ω_S . In order to define $\hat{f}^{\delta C}$ such that it satisfies the above requirements, consider first defining degree $p + 1$ correction functions $g_L = g_L(\xi)$ and $g_R = g_R(\xi)$ that approximate zero (in some sense) within Ω_S , as well as satisfying

$$g_L(-1) = 1, \quad g_L(1) = 0, \tag{12}$$

$$g_R(-1) = 0, \quad g_R(1) = 1, \tag{13}$$

and

$$g_L(\xi) = g_R(-\xi). \tag{14}$$

The exact form of g_L and g_R can be varied, determining various stability and accuracy properties; in this sense the FR approach can be considered a family of schemes. In particular, it has been shown that if g_L and g_R are the right and left Radau polynomials, respectively, then an under-integrated collocated-based nodal DG scheme is recovered (De Grazia et al., 2014; Huynh, 2007; Mengaldo et al., 2016), and if g_L and g_R are set to zero at a set of p points within Ω_S , located symmetrically about the origin, then SD schemes are recovered for a linear flux. A suitable expression for $\hat{f}^{\delta C}$ can now be written in terms of g_L and g_R as

$$\hat{f}^{\delta C} = (\hat{f}_L^{\delta I} - \hat{f}_L^{\delta D})g_L + (\hat{f}_R^{\delta I} - \hat{f}_R^{\delta D})g_R, \tag{15}$$

where $\hat{f}_L^{\delta D} = \hat{f}^{\delta D}(-1, t)$ and $\hat{f}_R^{\delta D} = \hat{f}^{\delta D}(1, t)$. Using this expression, the degree $p + 1$ approximate transformed total flux \hat{f}^{δ} within Ω_S can be constructed from the discontinuous and correction fluxes as follows

$$\hat{f}^{\delta} = \hat{f}^{\delta D} + \hat{f}^{\delta C} = \hat{f}^{\delta D} + (\hat{f}_L^{\delta I} - \hat{f}_L^{\delta D})g_L + (\hat{f}_R^{\delta I} - \hat{f}_R^{\delta D})g_R. \tag{16}$$

The final stage of the FR approach involves evaluating the divergence of \hat{f}^{δ} at each solution point ξ_i using the expression

$$\frac{\partial \hat{f}^{\delta}}{\partial \xi}(\xi_i) = \sum_{j=0}^k \hat{f}_j^{\delta D} \frac{dI_j}{d\xi}(\xi_i) + (\hat{f}_L^{\delta I} - \hat{f}_L^{\delta D}) \frac{dg_L}{d\xi}(\xi_i) + (\hat{f}_R^{\delta I} - \hat{f}_R^{\delta D}) \frac{dg_R}{d\xi}(\xi_i). \tag{17}$$

These values can then be used to advance $\hat{u}^{\delta D}$ in time via a suitable temporal discretisation of the following semi-discrete expression

$$\frac{d\hat{u}_i^{\delta D}}{dt} = - \frac{\partial \hat{f}^{\delta}}{\partial \xi}(\xi_i). \tag{18}$$

2.2 Advection Diffusion

Consider using the FR approach to solve Eq. (1) within an arbitrary 1D domain Ω , where x is a spatial coordinate, t is time, $u = u(x, t)$ is a conserved scalar quantity, and $f = f(u, q)$ is the flux of u in the x direction, where

$$q = \frac{\partial u}{\partial x}. \quad (19)$$

The first stage of the FR approach involves partitioning Ω into N distinct elements as per Eq. (2), and constructing approximations of the solution u in Eq. (1) and the flux f in Eq. (1) as per Eq. (3). Additionally, the so-called auxiliary variable q in Eq. (19) is approximated in each Ω_n by $q_n^{\delta D} = q_n^{\delta D}(x, t)$, which is a polynomial of degree p within Ω_n , and the solution u in Eq. (19) is approximated in each Ω_n by $u_n^\delta = u_n^\delta(x, t)$, which is a polynomial of degree $p + 1$ within Ω_n . Consequently, a total approximate auxiliary variable $q^{\delta D} = q^{\delta D}(x, t)$ and a total approximate solution $u^\delta = u^\delta(x, t)$ can be defined within Ω as

$$q^{\delta D} = \sum_{n=0}^{N-1} q_n^{\delta D} \approx q, \quad u^\delta = \sum_{n=0}^{N-1} u_n^\delta \approx u, \quad (20)$$

where no level of inter-element continuity in $q^{\delta D}$ is explicitly enforced. However, u^δ is required to be C_0 continuous at element interfaces.

The second stage of the FR approach involves transforming each Ω_n to a standard element Ω_S using the mapping defined by Eq. (4). This leads to Eqs. (21), (7), (8) as well as

$$\hat{q}^{\delta D} = \frac{\partial \hat{u}^\delta}{\partial x}, \quad (21)$$

where

$$\hat{q}^{\delta D} = \hat{q}^{\delta D}(\xi, t) = J_n^2 q_n^{\delta D}(\Gamma_n^{-1}(\xi), t) \quad (22)$$

is a polynomial of degree p , and

$$\hat{u}^\delta = \hat{u}^\delta(\xi, t) = J_n u_n^\delta(\Gamma_n^{-1}(\xi), t), \quad (23)$$

is a polynomial of degree $p + 1$.

The third stage of the FR approach involves defining the degree p polynomial $\hat{u}^{\delta D}$ in terms of a nodal basis as per Eq. (9).

The fourth stage of the FR approach involves calculating $\hat{u}^{\delta D}$ at the left- and right-hand ends of Ω_S , denoted \hat{u}_L^D and \hat{u}_R^D , respectively. These are subsequently used in conjunction with analogous information from adjoining elements to calculate common solution values at the left- and right-hand ends of Ω_S , denoted \hat{u}_L^l and \hat{u}_R^l , respectively. There are a number of approaches for determining common solution values, including the central flux (CF)

(Hesthaven and Warburton, 2008), local discontinuous Galerkin (LDG) (Cockburn and Shu, 1998), compact discontinuous Galerkin (CDG) (Peraire and Persson, 2008), internal penalty (IP) (Arnold, 1982), and the BR2 (Bassi and Rebay, 1997) approaches.

The fifth stage of the FR approach involves constructing the degree $p + 1$ polynomial \hat{u}^δ , by adding a correction flux $\hat{u}^{\delta C} = \hat{u}^{\delta C}(\xi, t)$ of degree $p + 1$ to $\hat{u}^{\delta D}$, such that their sum equals the transformed common solutions at $\xi = \pm 1$, yet in some sense follows $\hat{u}^{\delta D}$ within the interior of Ω_S . A suitable expression for $\hat{f}^{\delta C}$ can be written in terms of h_L and h_R , which have the same properties as g_L and g_R , respectively, as

$$\hat{u}^{\delta C} = (\hat{u}_L^{\delta I} - \hat{u}_L^{\delta D})g_L + (\hat{u}_R^{\delta I} - \hat{u}_R^{\delta D})g_R. \quad (24)$$

Using this expression the degree $p + 1$ approximate transformed total solution \hat{u}^δ within Ω_S can be constructed from the discontinuous and correction solutions as follows

$$\hat{u}^\delta = \hat{u}^{\delta D} + \hat{u}^{\delta C} = \hat{u}^{\delta D} + (\hat{u}_L^{\delta I} - \hat{u}_L^{\delta D})g_L + (\hat{u}_R^{\delta I} - \hat{u}_R^{\delta D})g_R. \quad (25)$$

The sixth stage of the FR approach involves constructing the degree p polynomial $\hat{q}^{\delta D}$. Using Eqs. (19), (25), (9) one can obtain

$$\hat{q}^{\delta D} = \sum_{i=0}^p \hat{u}_i^{\delta D} \frac{dI_i}{d\xi} + (\hat{u}_L^{\delta I} - \hat{u}_L^{\delta D}) \frac{dG_L}{d\xi} + (\hat{u}_R^{\delta I} - \hat{u}_R^{\delta D}) \frac{dG_R}{d\xi}. \quad (26)$$

The seventh stage of the FR approach involves constructing a degree p polynomial $\hat{f}^{\delta D} = \hat{f}^{\delta D}(\xi, t)$, defined as the approximate transformed discontinuous flux within Ω_S as per Eq. (11), where $\hat{f}_i^{\delta D} = \hat{f}_i^{\delta D}(t)$ at each solution point ξ_i now depend on both $\hat{u}^{\delta D}$ and $\hat{q}^{\delta D}$.

The eighth stage of the FR approach involves evaluating $\hat{u}^{\delta D}$ and $\hat{q}^{\delta D}$ at either end of the standard element Ω_S (i.e. at $\xi = \pm 1$). These values, in conjunction with analogous information from adjoining elements, are then used to calculate numerical interface fluxes. The exact methodology for calculating such numerical interface fluxes will depend on the nature of the equations being solved. For example, when solving the Navier–Stokes equations one may use a Roe type approximate Riemann solver (Roe, 1981) for the inviscid component, and one of the aforementioned CF, LDG, CDG, IP, or BR2 approaches for the viscous component. In what follows the numerical interface fluxes associated with the left- and right-hand ends of Ω_S (and transformed appropriately for use in Ω_S) will be denoted $\hat{f}_L^{\delta I}$ and $\hat{f}_R^{\delta I}$, respectively.

The penultimate stage of the FR approach involves constructing the degree $p + 1$ polynomial \hat{f}^δ as per Eq. (16), and the final stage of the FR approach involves evaluating the divergence of \hat{f}^δ at each solution point ξ_i as per Eq. (17). These values can then be used to advance $\hat{u}^{\delta D}$ in time via a suitable temporal discretisation of Eq. (18).

3 FR IN MULTIDIMENSIONS

3.1 Overview

In this section we will describe extension of the FR approach into two dimensions (2D) for both quadrilateral and triangular elements. The approaches presented further generalise into three dimensions and have been used successfully to obtain stable schemes inside of both hexahedra and tetrahedra. All discussions will be cast in terms of solving the following 2D scalar conservation law

$$\frac{\partial u}{\partial t} + \nabla_{xy} \cdot \mathbf{f} = 0 \quad (27)$$

within an arbitrary domain Ω , where x and y are spatial coordinates, t is time, $u = u(x, t)$ is a conserved scalar, $\mathbf{f} = (f, g)$ where $f = f(u)$ and $g = g(u)$ are the fluxes of u in the x and y directions, respectively.

3.2 Tensor Product Elements

Consider partitioning the domain Ω into N nonoverlapping, conforming quadrilateral elements Ω_n . To facilitate the implementation, each quadrilateral element Ω_n in the physical domain (x, y) is mapped to a reference element $\Omega_S = (\xi, \eta) | -1 \leq \xi, \eta \leq 1$ in the transformed space (ξ, η) .

Using this mapping, the governing equation in the physical domain can be transformed to an equivalent governing equation in the computational domain which takes the form

$$\frac{\partial \hat{u}}{\partial t} + \nabla_{\xi\eta} \cdot \hat{\mathbf{f}} = 0 \quad (28)$$

where

$$\hat{u} = Ju, \quad (29)$$

$$\hat{\mathbf{f}} = (\hat{f}, \hat{g}) = \left(\frac{\partial y}{\partial \eta} f - \frac{\partial x}{\partial \eta} g, -\frac{\partial y}{\partial \xi} f + \frac{\partial x}{\partial \xi} g \right), \quad (30)$$

$$J = \frac{\partial x \partial y}{\partial \xi \partial \eta} - \frac{\partial x \partial y}{\partial \eta \partial \xi}. \quad (31)$$

The approximate solution $\hat{u}^{\delta D}$ within the reference element Ω_S is represented by a multidimensional polynomial of degree p , defined by its values at a set of $N_p = (p+1)^2$ solution points. These solution points are generated by taking the tensor product of a set of 1D solution points. The approximate solution in the reference element takes the form

$$\hat{u}^{\delta D}(\mathbf{r}, t) = \sum_{i=1}^{p+1} \sum_{j=1}^{p+1} \hat{u}_{i,j}^{\delta D} l_i(\xi) l_j(\eta), \quad (32)$$

where $\{l_i\}$ are the set of 1D Lagrange polynomials associated with the set of solution points and $\hat{u}_{i,j}^{\delta D}$ is the value of the solution at the solution point located at (ξ_i, η_j) . Furthermore, a set of $p + 1$ flux points are located along each edge of the quadrilateral for a total of $4(p + 1)$ such points.

Following the 1D FR approach, the total transformed approximate flux $\hat{\mathbf{f}}^\delta = (\hat{f}^\delta, \hat{g}^\delta)$ is written as the sum of a discontinuous component $\hat{\mathbf{f}}^{\delta D}$ and a correction component $\hat{\mathbf{f}}^{\delta C}$,

$$\hat{\mathbf{f}}^\delta = \hat{\mathbf{f}}^{\delta D} + \hat{\mathbf{f}}^{\delta C}. \quad (33)$$

The approximate discontinuous flux $\hat{\mathbf{f}}^{\delta D} = (\hat{f}^{\delta D}, \hat{g}^{\delta D})$ is computed by constructing a degree p polynomial for each of its components as

$$\hat{\mathbf{f}}^{\delta D} = \sum_{i=1}^{p+1} \sum_{j=1}^{p+1} \hat{\mathbf{f}}_{i,j}^{\delta D} l_i(\xi) l_j(\eta), \quad (34)$$

where $\hat{\mathbf{f}}_{i,j}^{\delta D}$ is simply the value of the transformed flux evaluated directly at the solution point (ξ_i, η_j) .

The divergence of the discontinuous flux is therefore

$$\nabla_{\xi\eta} \cdot \hat{\mathbf{f}}^{\delta D} = \sum_{i=1}^{p+1} \sum_{j=1}^{p+1} \hat{f}_{i,j}^{\delta D} l'_i(\xi) l_j(\eta) + \sum_{i=1}^{p+1} \sum_{j=1}^{p+1} \hat{g}_{i,j}^{\delta D} l_i(\xi) l'_j(\eta), \quad (35)$$

where l'_i is the first derivative of l_i . The divergence of the transformed correction flux $\nabla_{\xi\eta} \cdot \hat{\mathbf{f}}^{\delta C} = \frac{\partial \hat{f}^{\delta C}}{\partial \eta} + \frac{\partial \hat{g}^{\delta C}}{\partial \xi}$ at solution point (ξ_i, η_i) is computed following the 1D methodology using

$$\frac{\partial \hat{f}^{\delta C}}{\partial \xi}(\xi_i, \eta_i) = \left((\hat{\mathbf{f}} \cdot \hat{\mathbf{n}})_L^{\delta I} - \hat{f}_L^{\delta D} \right) \frac{dh_L}{d\xi}(\xi_i) + \left((\hat{\mathbf{f}} \cdot \hat{\mathbf{n}})_R^{\delta I} - \hat{f}_R^{\delta D} \right) \frac{dh_R}{d\xi}(\xi_i), \quad (36)$$

$$\frac{\partial \hat{g}^{\delta C}}{\partial \eta}(\xi_i, \eta_i) = \left((\hat{\mathbf{f}} \cdot \hat{\mathbf{n}})_B^{\delta I} - \hat{g}_B^{\delta D} \right) \frac{dh_B}{d\eta}(\eta_j) + \left((\hat{\mathbf{f}} \cdot \hat{\mathbf{n}})_T^{\delta I} - \hat{g}_T^{\delta D} \right) \frac{dh_T}{d\eta}(\eta_j), \quad (37)$$

where $\hat{f}_L^{\delta D}$, $\hat{f}_R^{\delta D}$, $\hat{g}_L^{\delta D}$, and $\hat{g}_T^{\delta D}$ are the transformed discontinuous flux values at the flux points L , R , B , and T located at $(\xi, \eta) = (-1, \eta_j)$, $(1, \eta_j)$, $(\xi_i, -1)$, $(\xi_i, 1)$, respectively. The quantities $(\hat{\mathbf{f}} \cdot \hat{\mathbf{n}})_L^{\delta I}$, $(\hat{\mathbf{f}} \cdot \hat{\mathbf{n}})_R^{\delta I}$, $(\hat{\mathbf{f}} \cdot \hat{\mathbf{n}})_B^{\delta I}$, and $(\hat{\mathbf{f}} \cdot \hat{\mathbf{n}})_T^{\delta I}$ are the transformed common interface flux values at the flux points L , R , B , and T , respectively.

3.3 Simplex Elements

Consider partitioning the domain Ω into N nonoverlapping, conforming triangular elements Ω_n . To facilitate the implementation, each element Ω_n in

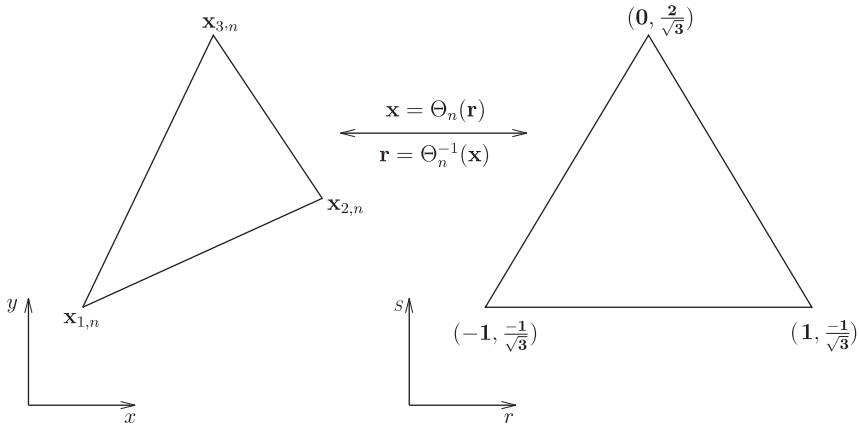


FIG. 1 Mapping between the physical space (x, y) and the computational space (r, s) . From the Ph.D. thesis of P. Castonguay and copyright P. Castonguay, reused with permission.

physical space is mapped to a reference equilateral triangle Ω_S , using a mapping Θ_n , as shown in Fig. 1.

For a linear triangular element, the mapping is

$$\mathbf{x} = \Theta_n(\mathbf{r}) = \frac{(-3r + 2 - \sqrt{3}s)}{6}\mathbf{x}_1 + \frac{(2 + 3r - \sqrt{3}s)}{6}\mathbf{x}_2 + \frac{(2 + 2\sqrt{3}s)}{6}\mathbf{x}_3 \quad (38)$$

where \mathbf{x}_1 , \mathbf{x}_2 , and \mathbf{x}_3 are the coordinates of the vertices of the triangular element Ω_n in physical space. Using this mapping, Eq. (27) in the physical domain can be transformed to an equivalent governing equation in the computational domain which takes the form

$$\frac{\partial \hat{u}}{\partial t} + \nabla_{rs} \cdot \hat{\mathbf{f}} = 0 \quad (39)$$

where

$$\hat{u} = Ju, \quad (40)$$

$$\hat{\mathbf{f}} = (\hat{f}, \hat{g}) = \left(\frac{\partial y}{\partial s} f - \frac{\partial x}{\partial s} g, -\frac{\partial y}{\partial r} f + \frac{\partial x}{\partial r} g \right), \quad (41)$$

$$J = \frac{\partial x \partial y}{\partial r \partial s} - \frac{\partial x \partial y}{\partial s \partial r}. \quad (42)$$

The approximate solution $\hat{u}^{\delta D}$ within the reference element Ω_S is represented by a multidimensional polynomial of degree p , defined by its values at a set of $N_p = (p+1)(p+2)/2$ solution points (represented by hollow circles in Fig. 2).

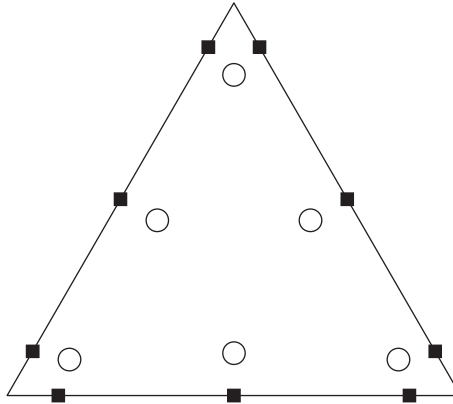


FIG. 2 Solution points (circles) and flux points (squares) in the reference element for $p = 2$. From the Ph.D. thesis of P. Castonguay and copyright P. Castonguay, reused with permission.

The approximate solution in the reference element takes the form

$$\hat{u}^{\delta D}(\mathbf{r}, t) = \sum_{i=1}^{N_p} \hat{u}_i^{\delta D} l_i(\mathbf{r}) \tag{43}$$

where $\hat{u}_i^{\delta D} = J_n \cdot u^{\delta D}(\Theta_n^{-1}(\mathbf{r}_i), t)$ is the value of \hat{u} at the solution point i of element n , and $l_i(\mathbf{r})$ is the multidimensional Lagrange polynomial associated with the solution point i in the reference equilateral triangle Ω_S . The approximate solution $\hat{u}^{\delta D}$ lies in the space $P_p(\Omega_S)$, defined as the space of polynomials of degree $\leq p$ on Ω_S . Following the 1D FR approach, the total transformed approximate flux $\hat{\mathbf{f}}^\delta = (\hat{f}^\delta, \hat{g}^\delta)$ is written as the sum of a discontinuous component $\hat{\mathbf{f}}^{\delta D}$ and a correction component $\hat{\mathbf{f}}^{\delta C}$,

$$\hat{\mathbf{f}}^\delta = \hat{\mathbf{f}}^{\delta D} + \hat{\mathbf{f}}^{\delta C}. \tag{44}$$

The approximate discontinuous flux $\hat{\mathbf{f}}^{\delta D} = (\hat{f}^{\delta D}, \hat{g}^{\delta D})$ is computed by constructing a degree p polynomial for each of its components as

$$\hat{f}^{\delta D} = \sum_{i=1}^{N_p} \hat{f}_i^{\delta D} l_i, \quad \hat{g}^{\delta D} = \sum_{i=1}^{N_p} \hat{g}_i^{\delta D} l_i \tag{45}$$

where the coefficients $\hat{f}_i^{\delta D}$ and $\hat{g}_i^{\delta D}$ are the values of the transformed flux at the solution point i evaluated directly from the approximate solution \hat{u} ($\hat{f}_i^{\delta D} = \hat{f}(\hat{u}_i)$ and $\hat{g}_i^{\delta D} = \hat{g}(\hat{u}_i)$). The divergence of the discontinuous flux is therefore

$$\nabla_{rs} \cdot \hat{\mathbf{f}}^{\delta D} = \sum_{i=1}^{N_p} \hat{f}_i^{\delta D} \frac{\partial l_i}{\partial r} + \sum_{i=1}^{N_p} \hat{g}_i^{\delta D} \frac{\partial l_i}{\partial s}. \tag{46}$$

On each edge of the element, a set of $N_{fp} = (p + 1)$ flux points are defined (illustrated by squares in Fig. 2) and used to couple the solution between neighbouring elements. The correction flux $\hat{\mathbf{f}}^{\delta C}$ is constructed as follows

$$\hat{\mathbf{f}}^{\delta C}(\mathbf{r}) = \sum_{f=1}^3 \sum_{j=1}^{N_{fp}} \left[(\hat{\mathbf{f}} \cdot \hat{\mathbf{n}})_{f,j}^{\delta I} - (\hat{\mathbf{f}}^{\delta D} \cdot \hat{\mathbf{n}})_{f,j} \right] \mathbf{h}_{f,j}(\mathbf{r}) \quad (47)$$

$$= \sum_{f=1}^3 \sum_{j=1}^{N_{fp}} \Delta_{f,j} \mathbf{h}_{f,j}(\mathbf{r}). \quad (48)$$

Regarding Eqs. (47) and (48), various points should be noted. First, expressions subscripted by the indices f, j correspond to a quantity at the flux point j of face f , where $1 \leq f \leq 3$ and $1 \leq j \leq N_{fp}$. The convention used to number the faces and flux points is illustrated in Fig. 3.

For example, $(\hat{\mathbf{f}}^{\delta D} \cdot \hat{\mathbf{n}})_{f,j}$ is the normal component of the discontinuous transformed flux $\hat{\mathbf{f}}^{\delta D}$ at the flux point f, j . In Eq. (47), $(\hat{\mathbf{f}} \cdot \hat{\mathbf{n}})_{f,j}^{\delta I}$ is a normal transformed numerical flux computed at flux point f, j . As in 1D FR, it is computed by first evaluating pairs of $u^{\delta D}$ at each flux point using Eq. (43). At each flux point, we define $u_-^{\delta D}$ to be the value of $u^{\delta D}$ computed using the information local to the current element and $u_+^{\delta D}$ to be the value of $u^{\delta D}$ computed using information from the neighbouring element sharing the same flux point. Once both approximate solution values ($u_-^{\delta D}$ and $u_+^{\delta D}$) are evaluated at each flux point, a system specific solver is used to compute a common interface flux based on $u_+^{\delta D}$, $u_-^{\delta D}$ and the local normal vector $\mathbf{n}_{f,j}$. From this common numerical flux, the transformed normal numerical flux denoted by $(\hat{\mathbf{f}} \cdot \hat{\mathbf{n}})_{f,j}^{\delta I}$ can be obtained. In Eq. (48), $\Delta_{f,j}$ is defined as the difference between the normal transformed numerical flux and the normal transformed discontinuous

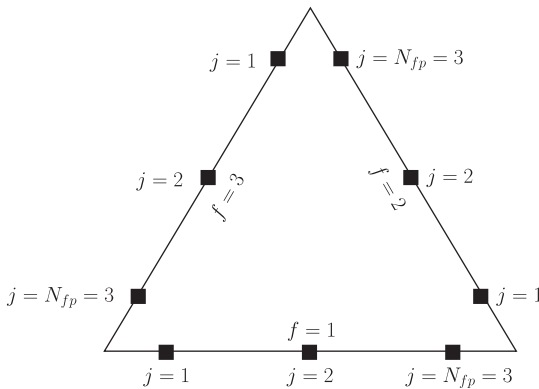


FIG. 3 Numbering convention for the faces and flux points on the reference triangular element. Example shown corresponds to $p = 2$. From the Ph.D. thesis of P. Castonguay and copyright P. Castonguay, reused with permission.

flux at the flux point f, j . Finally, $\mathbf{h}_{f, j}(\mathbf{r})$ is a vector correction function associated with flux point f, j . Each vector correction function $\mathbf{h}_{f, j}(\mathbf{r})$ is restricted to lie in the Raviart–Thomas space (Raviart and Thomas, 1977) of order p , denoted by $RT_p(\Omega_S)$. Because of this property,

$$\begin{aligned} \nabla_{rs} \cdot \mathbf{h}_{f, j} &\in P_p(\Omega_S) \\ \mathbf{h}_{f, j} \cdot \mathbf{n}|_{\Gamma_S} &\in R_p(\Gamma_S) \end{aligned} \tag{49}$$

where $P_p(\Omega_S)$ is the space of polynomials of degree $\leq p$ on the reference element Ω_S and $R_p(\Gamma_S)$ is the space of polynomials of degree $\leq p$ on the boundary of Γ_S . In other words, the divergence of each correction function ($\nabla_{rs} \cdot \mathbf{h}_{f, j}$) is a polynomial of degree p and the normal trace $\mathbf{h}_{f, j} \cdot \hat{\mathbf{n}}$ is also a polynomial of degree p along each edge. Furthermore, it is required that the correction functions $\mathbf{h}_{f, j}$ satisfy

$$\mathbf{h}_{f, j}(\mathbf{r}_{f_2, j_2}) \cdot \mathbf{n}_{f_2, j_2} = \begin{cases} 1 & \text{if } f=f_2 \text{ and } j=j_2 \\ 0 & \text{otherwise} \end{cases} \tag{50}$$

Hence, the following holds at each flux point f, j

$$\hat{\mathbf{f}}^{\delta C}(\mathbf{r}_{f, j}) \cdot \hat{\mathbf{n}}_{f, j} = \left[(\hat{\mathbf{f}} \cdot \hat{\mathbf{n}})_{f, j}^{\delta I} - (\hat{\mathbf{f}}^{\delta D} \cdot \hat{\mathbf{n}})_{f, j} \right] = \Delta_{f, j}. \tag{51}$$

An example of a vector correction function $\mathbf{h}_{f, j}$ is shown in Fig. 4 for the case $p = 2$. To simplify the notation in the following sections, the correction field $\phi_{f, j}(\mathbf{r})$ defined as the divergence of the correction function $\mathbf{h}_{f, j}(\mathbf{r})$ is introduced, i.e.

$$\phi_{f, j}(\mathbf{r}) = \nabla_{rs} \cdot \mathbf{h}_{f, j}(\mathbf{r}). \tag{52}$$

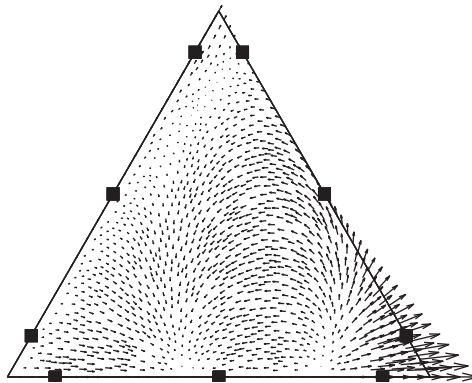


FIG. 4 A correction function associated with flux point $f = 2, j = 1$ for $p = 2$. From the Ph.D. thesis of P. Castonguay and copyright P. Castonguay, reused with permission.

Finally, combining Eqs. (39), (44), (46), and (48), the approximate solution values at the solution points can be updated from

$$\begin{aligned}
 \frac{d\hat{u}_i^\delta}{dt} &= -\left(\nabla_{rs} \cdot \hat{\mathbf{f}}^\delta\right)|_{\mathbf{r}_i} \\
 &= -\left(\nabla_{rs} \cdot \hat{\mathbf{f}}^{\delta D}\right)|_{\mathbf{r}_i} - \left(\nabla_{rs} \cdot \hat{\mathbf{f}}^{\delta C}\right)|_{\mathbf{r}_i} \\
 &= -\sum_{k=1}^{N_p} \hat{f}_k^{\delta D} \frac{\partial l_k}{\partial r} \Big|_{\mathbf{r}_i} - \sum_{k=1}^{N_p} \hat{g}_k^{\delta D} \frac{\partial l_k}{\partial s} \Big|_{\mathbf{r}_i} - \sum_{f=1}^3 \sum_{j=1}^{N_{fp}} \Delta_{f,j} \phi_{f,j}(\mathbf{r}_i).
 \end{aligned} \tag{53}$$

On triangular elements, the nature of a particular FR scheme depends on the location of the solution points, the location of the flux points, the methodology for calculating the transformed numerical interface flux $(\hat{\mathbf{f}} \cdot \hat{\mathbf{n}})_{f,j}^{\delta I}$, and finally, the form of the divergence $\phi_{f,j}$ of the correction functions $\mathbf{h}_{f,j}$. It has been shown in [Castonguay et al. \(2012\)](#) that a collocation-based (under integrated) nodal DG scheme is recovered on triangular elements if every correction function $\mathbf{h}_{f,j}$ is chosen such that

$$\int_{\Omega_S} \mathbf{h}_{f,j} \varphi d\Omega_S = 0 \tag{54}$$

for any polynomial $\varphi \in P_{p-1}(\Omega_S)$, i.e., the space of polynomials of degree $p - 1$. For further details, see [Castonguay et al. \(2012\)](#).

4 STABILITY AND ACCURACY OF FR SCHEMES

4.1 Energy Stability

[Jameson \(2010\)](#) proved that a particular SD scheme (recovered via FR) is energy-stable for linear advection problems in 1D. [Vincent et al. \(2011b\)](#) subsequently extended this result, and identified a family of stable FR schemes for linear advection problems in 1D for all orders of accuracy. Specifically, it was proven that if the left and right flux correction functions are defined as

$$g_L = \frac{(-1)^p}{2} \left[L_p - \left(\frac{\eta_p L_{p-1} + L_{p+1}}{1 + \eta_p} \right) \right], \tag{55}$$

$$g_R = \frac{1}{2} \left[L_p + \left(\frac{\eta_p L_{p-1} + L_{p+1}}{1 + \eta_p} \right) \right]. \tag{56}$$

where p is the degree of the solution polynomial within each element, L_{p-1} , L_p , and L_{p+1} are Legendre polynomials of the denoted degree (normalised such that $|L_p(\pm 1)| = 1$ for all p), and

$$\eta_p = \frac{c(2p+1)(a_p p!)^2}{2}, \tag{57}$$

with

$$a_p = \frac{(2p)!}{2^p (p!)^2}, \quad (58)$$

and c a free parameter in the range

$$\frac{-2}{(2p+1)(a_p p!)^2} < c < \infty, \quad (59)$$

then a broken Sobolev type norm of the discrete solution $\|u^{\delta D}\|_{p,2}$ with the from

$$\|u^\delta\|_{p,2} = \left[\sum_{n=0}^{N-1} \int_{x_n}^{x_{n+1}} (u_n^{\delta D})^2 + \frac{c}{2} (J_n)^{2p} \left(\frac{\partial^p u_n^{\delta D}}{\partial x^p} \right)^2 dx \right]^{1/2} \quad (60)$$

is guaranteed to be nonincreasing, and thus bounded. Consequently, by equivalence of norms in the finite-dimensional solution space, any norm of the solution is guaranteed to remain bounded, and thus the method is guaranteed to be stable. The resulting one parameter family of FR schemes, defined in terms of the free parameter c , have been referred to as Energy Stable Flux Reconstruction (ESFR) schemes. It can be noted that judicious choice of the parameter c leads to recovery of various known FR schemes. Specifically, if $c = 0$, then a particular nodal DG scheme is recovered, if

$$c = \frac{2p}{(2p+1)(p+1)(a_p p!)^2} \quad (61)$$

then a particular SD scheme is recovered (the scheme is, in fact, the particular SD scheme that (Huynh, 2007) showed to be Fourier stable, and Jameson (2010) proved to be energy stable), and if

$$c = \frac{2(p+1)}{(2p+1)p(a_p p!)^2} \quad (62)$$

then the g_2 FR scheme (Huynh, 2007) is recovered.

ESFR schemes for linear advection problems in 1D have been extended by Castonguay et al. (2012) to solve linear advection problems on 2D triangular grids. As in the 1D case, a one-parameter family of correction functions were identified that guarantee a particular norm of the solution is nonincreasing. However, unlike in the 1D case, an explicit expression for these correction functions was not presented (instead the divergence of each correction function was defined implicitly via a matrix system). Interestingly, the one-parameter family of schemes did not appear to include an SD scheme as a special case, despite the fact that Balan et al. (2011) were able to identify stable SD schemes on triangular grids for several orders or accuracy. The 1D ESFR schemes have also been extended by Sheshadri and Jameson (2016) to solve linear advection problems on tensor-product quadrilateral elements.

Williams et al. (2013), Castonguay et al. (2013), and Williams and Jameson (2013) have extended ESFR schemes for linear advection problems to develop a range of ESFR schemes for linear advection–diffusion problems on multiple element types. Their approach involves use of ESFR correction functions to construct a continuous polynomial representation of the solution (in addition to a continuous representation of the flux) within each element. Development of an energy-stable treatment for diffusive terms is important, since it is a prerequisite for effective solution of the Navier–Stokes equations.

4.2 von Neumann Analysis

Energy-based stability proofs are powerful since they apply for all orders of accuracy and on nonuniform grids. However, they do not offer insight into all the stability properties of a numerical scheme. Huynh (2007) and Vincent et al. (2011a) presented comprehensive von Neumann analyses of FR methods in order to elucidate further stability properties of the schemes. Their results indicate that the form of the flux correction function has a significant impact on the CFL stability limit associated with a given FR scheme. In the context of 1D ESFR schemes for linear advection, it has been shown that increasing the free parameter c (from zero) can increase the CFL limit by over a factor of two in certain cases. However, this is at the cost of a reduction in the overall accuracy of the scheme.

It has been observed that FR schemes can achieve the expected $p + 1$ order of accuracy for a variety of problems, much like nodal DG schemes (Hesthaven and Warburton, 2008). Additionally, von Neumann analysis has shown that FR schemes can in theory achieve so-called super-accuracy for dispersion and dissipation errors in the asymptotic ‘well-resolved’ limit, up to order $2p + 1$ (Huynh, 2007; Vincent et al., 2011a). Such super-accuracy has been demonstrated for the solution on 2D structured grids (Vincent et al., 2011a). However, the extent to which it extends to unstructured meshes is yet to be determined. Moreover, it has also been found by von Neumann analysis that steady state solutions are limited to accuracy of order $p + 1$ (Asthana et al., 2016).

More recently Li and Wang (2013) have used von Neumann analysis to develop FR methods optimised for aeroacoustics, and Asthana and Jameson (2015) have used von Neumann analysis to derive a set of spectrally optimal FR schemes, designed to minimise wave propagation error across all resolvable wavenumbers. These schemes were found to yield an improvement over collocation-based nodal DG.

4.3 Nonlinear Stability

Jameson et al. (2011) and Mengaldo et al. (2015) showed that FR methods can be afflicted by an aliasing driven instability if the flux function is nonlinear. Such instabilities are a consequence of aliasing errors (that occur when a

polynomial representation of the nonlinear flux is constructed via a collocation projection at the solution points). Jameson et al. (2011) also demonstrated that the location of the solution points plays a critical role in determining the extent of any aliasing driven instabilities. Specifically, they suggest that the solution points should be located at the abscissa of a strong quadrature rule in order to minimise aliasing driven instabilities. This finding is supported by the numerical experiments of Castonguay et al. (2011), who used the FR approach to solve the Euler equations on 2D triangular grids. They found that if the solution points were located at the so-called alpha-optimised points of Hesthaven and Warburton (2008) then the simulations blew up. However, if the solution points were located at the abscissa of a high-strength quadrature rule derived by Taylor et al. (2005), then the simulations remained stable. More recent works by Witherden and Vincent (2014) and Witherden et al. (2016) have further validated this hypothesis. However, it is unclear if, for a given element type, there exists an optimal set of solution points for a range of flow problems.

Other efforts to improve nonlinear stability have included development of limiting strategies for dealing with shocks (Park and Kim, 2016), as well as derivation of summation-by-parts operators for FR (Ranocha et al., 2016); an approach which has previously yielded successful results in a DG context (Gassner, 2013).

5 IMPLEMENTATION

5.1 Overview

In addition to offering high-order accuracy on unstructured mixed grids, FR schemes are also compact in space, and thus when combined with explicit time marching offer a significant degree of element locality. As such, explicit high-order FR schemes are characterised by a large degree of structured computation, even on unstructured grids. Over the past two decades improvements in the arithmetic capabilities of processors have significantly outpaced advances in random access memory. Algorithms which have traditionally been compute bound—such as dense matrix-vector products—are now limited instead by the bandwidth to/from memory. Whereas the CPUs of two decades ago had FLOPS-per-byte of 0.2 more recent chips have ratios upwards of 4. This disparity is not limited to just conventional CPUs. Massively parallel accelerators and coprocessors such as the Nvidia K20X and Intel Xeon Phi 5110P have ratios of 5.24 and 3.16, respectively.

A concomitant of this disparity is that modern hardware architectures are highly dependent on a combination of high-speed caches and/or shared memory to maintain throughput. However, for an algorithm to utilise these efficiently its memory access pattern must exhibit a degree of either spatial or temporal locality. To a first-order approximation the spatial locality of a

method is inversely proportional to the amount of memory indirection. On an unstructured grid indirection arises whenever there is coupling between elements. This is potentially a problem for discretisations whose stencil is not compact. Coupling also arises in the context of implicit time stepping schemes. Implementations are therefore very often bound by memory bandwidth. As a secondary trend we note that the manner in which FLOPS are realised has also changed. In the early 1990s commodity CPUs were predominantly scalar with a single core of execution. However, in 2015 processors with eight or more cores are not uncommon. Moreover, the cores on modern processors almost always contain vector processing units. Vector lengths of 512-bits, which permit up to eight double precision values to be operated on at once, will soon be commonplace. It is therefore imperative that compute-bound algorithms are amenable to both multithreading and vectorisation. A versatile means of accomplishing this is by breaking the computation down into multiple, necessarily independent, streams. By virtue of their independence these streams can be readily divided up between cores and vector lanes. This leads directly to the concept of stream processing. A corollary of the above discussion is that compute intensive discretisations which can be formulated within the stream processing paradigm are well suited to acceleration on current and likely future hardware platforms. The FR approach combined with explicit time-stepping is an archetypical of this.

5.2 Salient Aspects of an FR Implementation

The majority of operations within an FR time-step can be cast in terms of matrix–matrix multiplications, in which a fixed, small, approximately square, and sometimes sparse operator matrix multiplies a dynamic, large, ‘short-fat’, dense state matrix (such multiplies are often referred to as block-by-panel). All remaining operations (e.g. flux evaluations) are point-wise, concerning themselves with either a single solution point inside of an element or two collocating flux points at an interface. Hence, in broad terms, there are five salient aspects of an FR implementation, specifically (i) definition of the constant operator matrices, (ii) specification of the state matrices, (iii) implementation of matrix multiply kernels, (iv) implementation of point-wise kernels, and finally (v) handling of distributed memory parallelism and scheduling of kernel invocations. For full details of a particular cross-platform implementation called PyFR, which has exhibited performance at around 50% of machine peak in benchmark calculations on massively parallel GPU-based clusters see [Witherden et al. \(2014\)](#) and [Vincent et al. \(2015\)](#).

It is often convenient to defer matrix multiplications to the GEMM family of subroutines from a suitable Basic Linear Algebra Subprograms (BLAS) library. BLAS is available for virtually all platforms and optimised versions are often maintained by the hardware vendors themselves (e.g., cuBLAS for Nvidia GPUs). This approach greatly facilitates development of efficient and platform portable code. We note, however, that the matrix sizes

encountered in FR are not necessarily optimal from a GEMM perspective. Specifically, GEMM is optimised for the multiplication of large square matrices, whereas the constant operator matrixes in FR are ‘small and square’ with 10–100 rows/columns, and the state matrices are ‘short and fat’ with 10–100 rows and 10,000–100,000 columns. Moreover, we note that the constant operator matrices are know a priori and do not change in time. This a priori knowledge can be leveraged to design bespoke matrix multiply kernels that are more efficient than GEMM. The GiMMiK project is an example of such an approach (Wozniak et al., 2016) and has been found to improve performance by factors of two or more.

6 APPLICATIONS

In this section we will demonstrate some applications of the FR approach to solving nonlinear systems in three dimensions. Specifically, we will showcase how FR has been used to solve the compressible Euler and Navier–Stokes equations for three benchmark problems: flow over a circular cylinder, flow around an SD7003 wing, and flow through a T106c low-pressure turbine cascade.

6.1 Solving the Euler and Navier–Stokes Equations

The Navier–Stokes equations govern the dynamics for compressible flow. In the case where the flow is inviscid they reduce to the Euler equations. Both sets of equations take the form of nonlinear conservation laws. The FR approach can be readily extended to solve such systems by applying the approaches prescribed above for scalar FR to each component in the system.

In conservative form the Euler equations can be expressed as

$$\frac{\partial u}{\partial t} + \nabla \cdot f(u) = 0, \quad (63)$$

where

$$u = \begin{Bmatrix} \rho \\ \rho v_x \\ \rho v_y \\ \rho v_z \\ E \end{Bmatrix}, \quad f = f^{(\text{inv})} = \begin{Bmatrix} \rho v_x & \rho v_y & \rho v_z \\ \rho v_x^2 + p & \rho v_y v_x & \rho v_z v_x \\ \rho v_x v_y & \rho v_y^2 + p & \rho v_z v_y \\ \rho v_x v_z & \rho v_y v_z & \rho v_z^2 + p \\ v_x(E + p) & v_y(E + p) & v_z(E + p) \end{Bmatrix}, \quad (64)$$

here ρ is the mass density of the fluid, $\mathbf{v} = (v_x, v_y, v_z)^T$ is the fluid velocity vector, E is the total energy per unit volume and p is the pressure. For a perfect gas the pressure and total energy can be related by the ideal gas law

$$E = \frac{p}{\gamma - 1} + \frac{1}{2} \rho \|\mathbf{v}\|^2, \quad (65)$$

where $\gamma = c_p/c_v$ is the ratio of specific heats.

The more general Navier–Stokes equations can be written as an extension of the Euler equations through the inclusion of viscous terms. Within the presentation outlined above the flux now takes the form of $\mathbf{f} = \mathbf{f}^{(\text{inv})} - \mathbf{f}^{(\text{vis})}$ where

$$\mathbf{f}^{(\text{vis})} = \left\{ \begin{array}{ccc} 0 & 0 & 0 \\ \mathcal{T}_{xx} & \mathcal{T}_{yx} & \mathcal{T}_{zx} \\ \mathcal{T}_{xy} & \mathcal{T}_{yy} & \mathcal{T}_{zy} \\ \mathcal{T}_{xz} & \mathcal{T}_{yz} & \mathcal{T}_{zz} \\ \sum_i v_i \mathcal{T}_{ix} + \Delta \partial_x T & \sum_i v_i \mathcal{T}_{iy} + \Delta \partial_y T & \sum_i v_i \mathcal{T}_{iz} + \Delta \partial_z T \end{array} \right\}. \quad (66)$$

In the above we have defined $\Delta = \mu c_p / P_r$, where μ is the dynamic viscosity and P_r is the Prandtl number. The components of the stress-energy tensor are given by

$$\mathcal{T}_{ij} = \mu(\partial_i v_j + \partial_j v_i) - \frac{2}{3} \mu \delta_{ij} \nabla \cdot \mathbf{v}, \quad (67)$$

where δ_{ij} is the Kronecker delta. Using the ideal gas law the temperature can be expressed as

$$T = \frac{1}{c_v \gamma - 1} \frac{p}{\rho}, \quad (68)$$

with partial derivatives thereof being given according to the quotient rule.

6.2 Flow Over a Circular Cylinder

Flow over a circular cylinder has been the focus of various experimental and numerical studies (Breuer, 1998; Kravchenko and Moin, 2000; Ma et al., 2000; Norberg, 1998; Parnaudeau et al., 2008; Vermeire and Nadarajah, 2013, 2015). Characteristics of the flow are known to be highly dependent on the Reynolds number Re , defined as

$$Re = \frac{u_\infty D}{\nu}, \quad (69)$$

where u_∞ is the free-stream fluid speed, D is the cylinder diameter, and ν is the fluid kinematic viscosity. Roshko (1953) identified a stable range between $Re = 40$ and 150 that is characterised by the shedding of regular laminar vortices, as well as a transitional range between $Re = 150$ and 300 , and a turbulent range beyond $Re = 300$. These results were subsequently confirmed by Bloor (1964), who identified a similar set of regimes. Later, Williamson (1988) identified two modes of transition from two- to three-dimensional flow. The first, known as Mode-A instability, occurs at $Re \approx 190$ and the second, known as Mode-B instability, occurs at $Re \approx 260$. The turbulent range beyond

$Re = 300$ can be further subclassified into the shear-layer transition, critical, and supercritical regimes as discussed in the review by [Williamson \(1996\)](#).

Previous studies of [Witherden et al.](#) have used the FR approach to simulate flow over a circular cylinder at $Re = 3900$, and an effectively incompressible Mach number of 0.2. This case sits in the shear-layer transition regime identified by [Williamson \(1996\)](#), and contains several complex flow features, including separated shear layers, turbulent transition, and a fully turbulent wake. In addition to the recent study of [Witherden et al.](#) this test case has also been the focus of a number of other works, both experimental and numerical ([Breuer, 1998](#); [Kravchenko and Moin, 2000](#); [Ma et al., 2000](#); [Norberg, 1998](#); [Parnaudeau et al., 2008](#)). In 2013, [Lehmkuhl et al.](#) demonstrated that the wake profile for this test case can be classified as one of two modes, a low-energy mode (Mode-L) and a high-energy mode (Mode-H). Specifically, via analysis of a very long period simulation (over 2000 convective times), they showed that the wake fluctuates between these two modes.

6.2.1 Domain and Mesh

In their study [Witherden et al. \(2015\)](#) used a computational domain of dimensions $[-9D, 25D]$; $[-9D, 9D]$; and $[0, \pi D]$ in the stream-, cross-, and span-wise directions, respectively. The cylinder is centred at $(0, 0, 0)$. The stream-wise and cross-wise dimensions are comparable to the experimental and numerical values used by [Parnaudeau et al. \(2008\)](#). The overall domain dimensions are also comparable to those used for DNS studies by [Lehmkuhl et al. \(2013\)](#). The domain is periodic in the span-wise direction, with a no-slip isothermal wall boundary condition applied at the surface of the cylinder, and Riemann invariant boundary conditions applied at the far-field.

In the study, the domain was meshed in two ways. The first mesh consisted of entirely structured hexahedral elements, while the second was unstructured, consisting of prismatic elements in the near wall boundary layer region, and tetrahedral elements in the wake and far-field. Both meshes employed quadratically curved elements and were designed to fully resolve the near wall boundary layer region when $p = 4$. Specifically, the maximum skin friction coefficient was estimated a priori as $C_f \approx 0.075$ based on the LES results of [Breuer \(1998\)](#). The height of the first element was then specified such that when $p = 4$ the first solution point from the wall sits at $y^+ \approx 1$, where nondimensional wall units are calculated in the usual fashion as $y^+ = u_\tau y / \nu$ with $u_\tau = \sqrt{C_f / 2} u_\infty$.

The hexahedral mesh had 104 elements in the circumferential direction, and 16 elements in the span-wise direction, which when $p = 4$ achieves span-wise resolution comparable to that used in previous studies. The prism/tetrahedral mesh has 116 elements in the circumferential direction, and 20 elements in the span-wise direction, these numbers being chosen to help reduce face aspect ratios at the edges of the prismatic layer; which

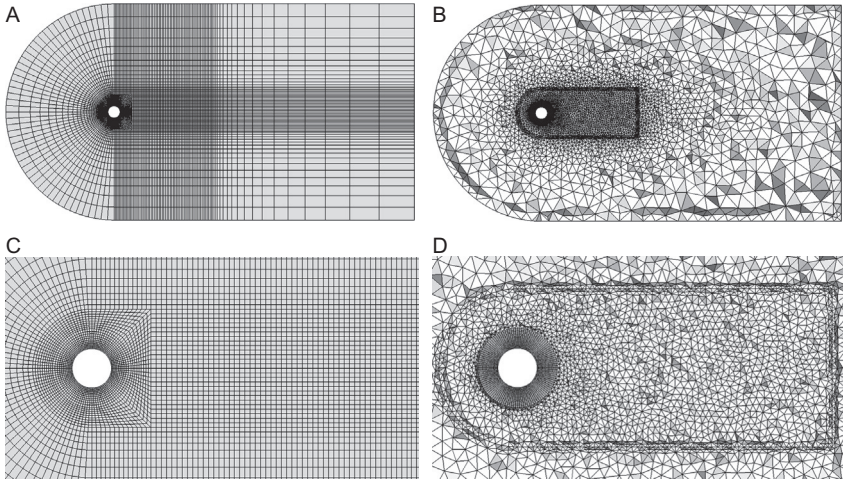


FIG. 5 Cutaways through the two meshes. (A) Hexahedral, far-field. (B) Prism/tetrahedral, far-field. (C) Hexahedral, wake. (D) Prism/tetrahedral, wake. *From Witherden, F.D., Vermeire, B.C., Vincent, P.E., 2015. Heterogeneous computing on mixed unstructured grids with PyFR. Comput. Fluids 120, 173–186, and copyright F.D. Witherden, B.C. Vermeire, P.E. Vincent, reused with permission.*

facilitates transition to the fully unstructured tetrahedral elements in the far-field. In total the hexahedral mesh contained 119,776 elements, and the prism/tetrahedral mesh contained 79,344 prismatic elements and 227,298 tetrahedral elements. Both meshes are shown in Fig. 5.

6.2.2 Methodology

The compressible Navier–Stokes equations, with constant viscosity, were solved on each of the two meshes shown in Fig. 5. A DG scheme was used for the spatial discretisation, a Rusanov Riemann solver was used to calculate the inviscid fluxes at element interfaces, and the explicit RK45[2R+] scheme of Kennedy et al. (2000) was used to advance the solution in time. No subgrid model was employed, hence the approach should be considered ILES/DNS (Vermeire et al., 2013, 2014), as opposed to classical LES.

6.2.3 Accuracy

In this section we present the time-span-averaged results obtained by Witherden et al. using a cluster of 12 NVIDIA K20c GPUs at $p = 4$, the design resolution for both meshes. Both simulations were run for 1000 convective times, allowing the flow to fluctuate between Mode-H and Mode-L as identified by Lehmkühl et al. (2013) and Ma et al. (2000). A moving window time-average with a width of 100 convective times is used to extract both modes from the long-period simulation. This yields four datasets including both Mode-H and Mode-L for both

the hexahedral and prism/tetrahedral meshes. Both modes are then compared with results from previous experimental and numerical studies, where either one or both of the modes were observed (Lehmkuhl et al., 2013; Ma et al., 2000; Norberg, 1998; Parnaudeau et al., 2008).

Instantaneous surfaces of iso-density are shown in Fig. 6 for both simulations at similar phases of the shedding cycle. We observe laminar flow at the leading edge of the cylinder for both test cases, turbulent transition near the separation points, and fully turbulent flow in the wake region. These are the characteristic features of the shear-layer transition regime, as described by Williamson (1996). The wake is composed of large vortices, alternately shedding off of the upper and lower surfaces of the cylinder, and smaller scale turbulent structures.

Plots of the averaged stream-wise wake profiles are shown in Figs. 7 and 8 for Mode-H and Mode-L, respectively. Both the hexahedral and prism/tetrahedral meshes show excellent agreement with the numerical results of Lehmkuhl et al. (2013) for both modes and with the experimental results of Parnaudeau et al. (2008), which is available for Mode-L. The Mode-H cases exhibit relatively shorter separation bubbles and the Mode-L cases have characteristic inflection points in the wake profile near $x/D \approx 1$.

Plots of the averaged pressure coefficient $\overline{C_p}$ on the surface of the cylinder are shown in Figs. 9 and 10 for both extracted modes and both meshes. The Mode-H results are shown alongside the Mode-H numerical results of Lehmkuhl et al. (2013) and the results from Case I of Ma et al. (2000). The Mode-L results are shown alongside the Mode-L numerical results of Lehmkuhl et al. (2013) and the experimental results of Norberg (1998) at a similar $Re = 4020$, which were extracted from Kravchenko and Moin (2000). Both modes have similar pressure coefficient distributions at the leading face of the cylinder, while the Mode-H case has stronger suction on the trailing face adjacent to the separation bubble. Both modes extracted using both meshes show excellent agreement with their corresponding reference data sets (Table 1).

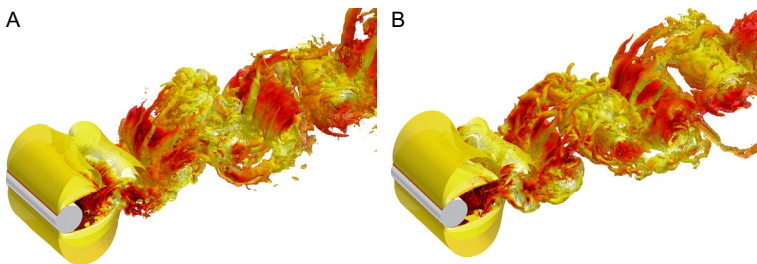


FIG. 6 Instantaneous surfaces of iso-density coloured by velocity magnitude. (A) Structured hexahedral. (B) Unstructured prism/tetrahedral. From Witherden, F.D., Vermeire, B.C., Vincent, P.E., 2015. *Heterogeneous computing on mixed unstructured grids with PyFR*. *Comput. Fluids* 120, 173–186, and copyright F.D. Witherden, B.C. Vermeire, P.E. Vincent, reused with permission.

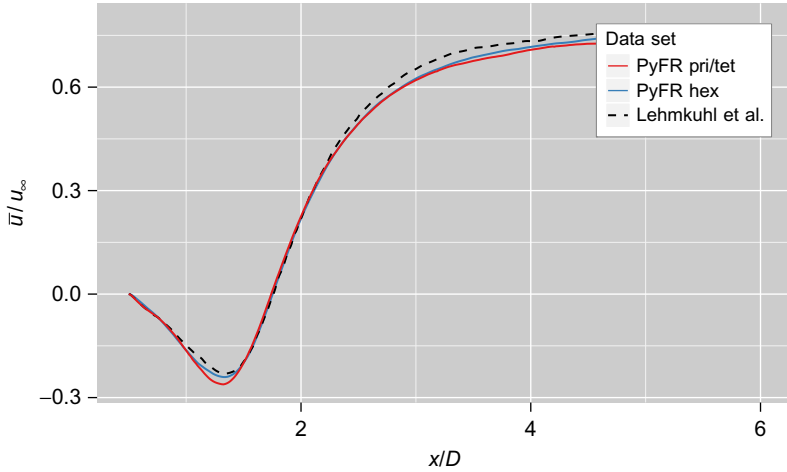


FIG. 7 Averaged wake profiles for Mode-H compared with the numerical results of [Lehmkuhl et al. \(2013\)](#). From [Witherden, F.D., Vermeire, B.C., Vincent, P.E., 2015. Heterogeneous computing on mixed unstructured grids with PyFR. *Comput. Fluids* 120, 173–186, and copyright F.D. Witherden, B.C. Vermeire, P.E. Vincent, reused with permission.](#)

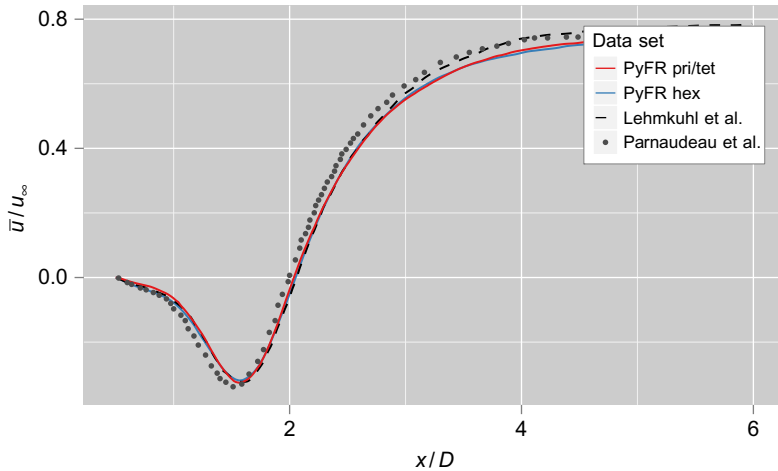


FIG. 8 Averaged wake profiles for Mode-L compared with the numerical results of [Lehmkuhl et al. \(2013\)](#) and experimental results of [Parnaudeau et al. \(2008\)](#). From [Witherden, F.D., Vermeire, B.C., Vincent, P.E., 2015. Heterogeneous computing on mixed unstructured grids with PyFR. *Comput. Fluids* 120, 173–186, and copyright F.D. Witherden, B.C. Vermeire, P.E. Vincent, reused with permission.](#)

The averaged pressure coefficient at the base of the cylinder $\overline{C_{pb}}$, and the averaged separation angle θ_s measured from the leading stagnation point are tabulated in [Fig. 1](#) for both modes and meshes. These are shown along with measurements from the experimental results of [Norberg \(1998\)](#), experimental data from [Parnaudeau et al. \(2008\)](#), and DNS data from [Lehmkuhl et al. \(2013\)](#) for

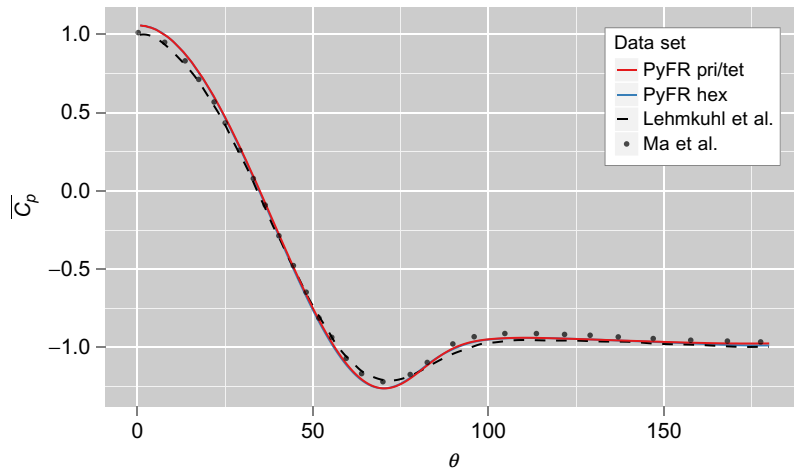


FIG. 9 Averaged pressure coefficient for Mode-H compared with the numerical results of [Ma et al. \(2000\)](#) and [Lehmkuhl et al. \(2013\)](#). From [Witherden, F.D., Vermeire, B.C., Vincent, P.E., 2015. Heterogeneous computing on mixed unstructured grids with PyFR. *Comput. Fluids* 120, 173–186, and copyright F.D. Witherden, B.C. Vermeire, P.E. Vincent, reused with permission.](#)

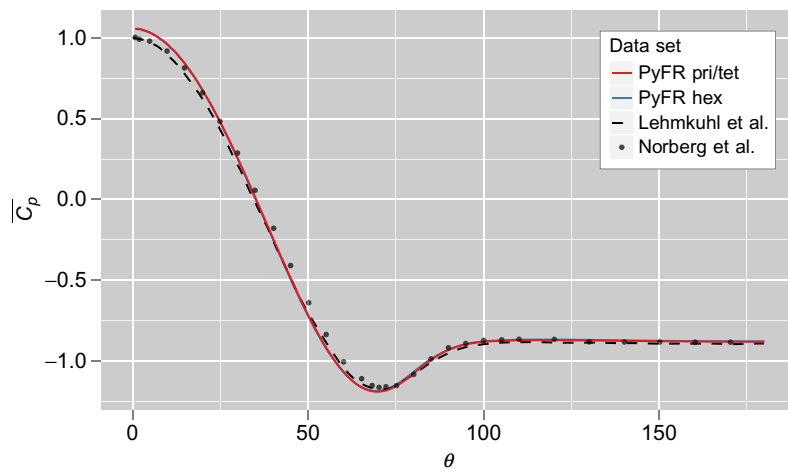


FIG. 10 Averaged pressure coefficient for Mode-L compared with the numerical results of [Lehmkuhl et al. \(2013\)](#) and experimental results of [Norberg \(1998\)](#). From [Kravchenko, A.G., Moin, P., 2000. Numerical studies of flow over a circular cylinder at \$Re_d = 3\,900\$. *Phys. Fluids* 12, 403–417 and \[Witherden, F.D., Vermeire, B.C., Vincent, P.E., 2015. Heterogeneous computing on mixed unstructured grids with PyFR. *Comput. Fluids* 120, 173–186, and copyright F.D. Witherden, B.C. Vermeire, P.E. Vincent, reused with permission.\]\(#\)](#)

TABLE 1 Comparison of Quantitative Values With Experimental and DNS Results

	Mode-H		Mode-L	
	$-\overline{C_{pb}}$	$\theta_s/\text{degrees}$	$-\overline{C_{pb}}$	$\theta_s/\text{degrees}$
PyFR Pri/tet	0.974	87.13	0.882	86.90
PyFR Hex	0.987	88.28	0.880	87.71
Parnaudeau et al. (2008)				88.00
Lehmkuhl et al. (2013)	0.980	88.25	0.877	87.80
Norberg (1998) (extracted from Kravchenko and Moin, 2000)			0.880	

both modes. Both measured quantities agree well with the reference data sets for both modes and meshes. The difference in separation angle is less than ~ 1 degree between the current and reference results. The pressure coefficient at base of the cylinder shows that the high-energy Mode-H case has stronger recirculation in the wake, characterised by greater suction at the wall adjacent to the recirculation bubble.

6.3 Flow Over an SD7003 Wing

Both Vermeire et al. (2016) and Williams (2013) have used FR schemes to simulate flow over an SD7003 infinite wing at 4 degrees angle of attack. The SD7003 geometry is that of a low Reynolds number Selig/Donovan airfoil that has a maximum thickness of 9.2% at 30.9% chord, and a maximum camber of 1.2% at 38.3% chord.

The numerical experiments of Williams on the SD7003 geometry were performed on a cylindrical domain formed by extruding a circular domain (of radius $20c$) by $0.2c$ in the z direction where c is the chord. Periodic boundary conditions were prescribed on the front and back of the cylindrical domain, characteristic boundary conditions were prescribed on the sides of the domain, and adiabatic wall boundary conditions were prescribed on the surface of the wing-section. The domain was then meshed with 711,332 quadratically curved tetrahedral elements.

The Reynolds number was taken to be $Re = 10,000$ with the incoming flow having a velocity of Mach $M = 0.2$. The angle of entry for the incoming flow was set as 4 degree in order to simulate a 4 degree angle of attack. The simulations were run using two different tetrahedral ESFR schemes: one with

$c = 0$ designed to recover a collocated nodal DG scheme and another with $c = c^+$ where c^+ is chosen to maximise the permissible explicit time step. The solution was marched forward in time using the RK54 approach and, at each time-step, the inviscid and viscous numerical fluxes were computed using a Rusanov-type Riemann solver. Results were evaluated after the lift and drag reached a pseudo-periodic state.

Lift and drag results for the two simulations of Williams along with the numerical results of [Uranga et al. \(2011\)](#) can be seen in [Table 2](#). Looking at the table it can be seen that both ESFR schemes show good agreement with the coefficients obtained by Uranga et al. The time history of the lift C_L and drag C_D coefficients for the $c = c^+$ simulation are shown in [Fig. 11](#). Instantaneous isosurfaces of density and vorticity for this simulation are shown in [Fig. 12](#).

TABLE 2 Time Averaged Lift $\overline{C_L}$ and Drag $\overline{C_D}$ Coefficients of Williams for the SD7003 Wing at $Re = 10,000$ and $M = 0.2$ Using $p = 3$ Tetrahedral ESFR Schemes

Simulation	$\overline{C_L}$	$\overline{C_D}$
Uranga et al. (2011)	0.3743	0.04967
Williams $c = 0$	0.3466	0.04908
Williams $c = c^+$	0.3454	0.04903

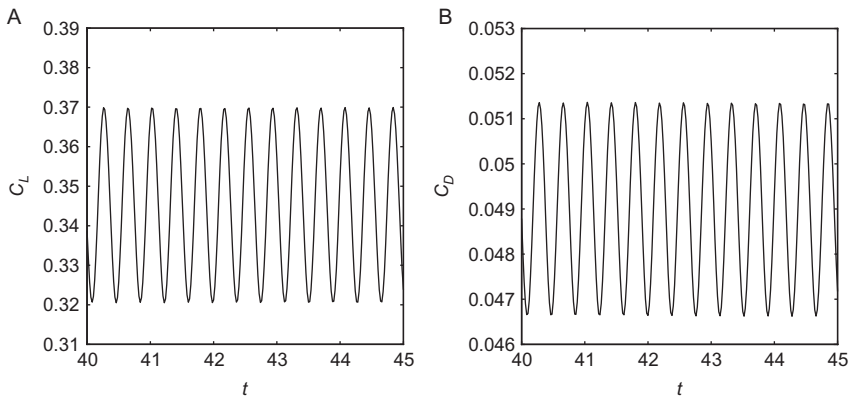


FIG. 11 Temporal variation of the lift and drag coefficients for the SD7003 wing at $Re = 10,000$ and $M = 0.2$ using $p = 3$ tetrahedral ESFR scheme with $c = c^+$. (A) Lift coefficient. (B) Drag coefficient. From Williams, D.M., 2013. *Energy stable high-order methods for simulating unsteady, viscous, compressible flows on unstructured grids* (Ph.D. thesis), Stanford University, and copyright D.M. Williams, reused with permission.

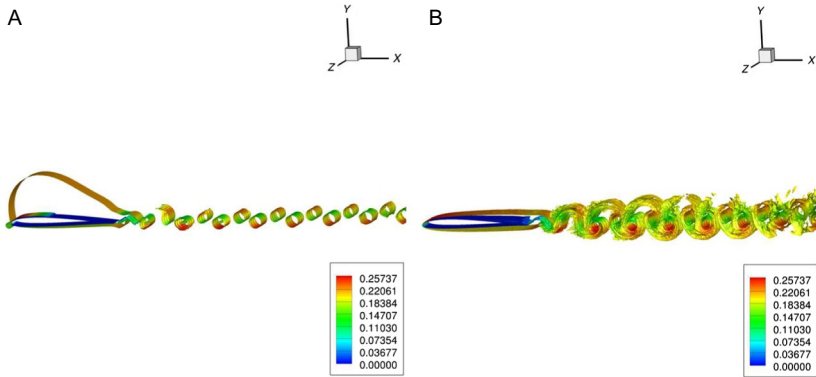


FIG. 12 Instantaneous isosurfaces of density and vorticity, coloured by Mach number, for the SD7003 wing at $Re = 10,000$ and $M = 0.2$ using $p = 3$ tetrahedral ESFR scheme with $c = c^+$. (A) Density isosurfaces. (B) Vorticity isosurfaces. *From Williams, D.M., 2013. Energy stable high-order methods for simulating unsteady, viscous, compressible flows on unstructured grids (Ph.D. thesis), Stanford University, and copyright D.M. Williams, reused with permission.*

6.4 T106c Low-Pressure Turbine Cascade

FR schemes have also shown promise in simulating flows over turbomachinery. The T106 low-pressure turbine cascade (Wood et al., 1990) is a popular test case for evaluating CFD solvers. The T106c cascade is defined by imposing a pitch-to-cord ratio of $s/c = 0.95$ and is supported by a wide body of numerical and experimental data (Garai et al., 2016; Hillewaert et al., 2014; Michlek et al., 2012; Pacciani et al., 2011). From the specification of the T106c cascade the chord is $c = 0.09301$ m and the pitch-wise inlet flow angle is 32.7 degree. In this study we will consider the case at Reynolds number $Re = 80,000$, with an outlet Mach number of $M = 0.65$. These conditions are of interest as they represent a fully compressible simulation at a meaningful Reynolds number. The working fluid for the case is taken to be air with a total temperature at the inlet of $T_i = 298.15$ K. The ratio of specific heats is $\gamma = 1.4$ with the specific gas constant being given by $R \simeq 287.1$ J kg⁻¹ K⁻¹.

Additional characteristics of the flow can be determined using the isentropic flow equations. The exit temperature can be determined as

$$T_e = \frac{T_i}{1 + \frac{\gamma - 1}{2} M^2} \simeq 274.92 \text{ K}, \quad (70)$$

with the exit velocity being given by

$$v_e = M \sqrt{\gamma R T_e} \simeq 216.07 \text{ m s}^{-1}. \quad (71)$$

Using Sutherland's law the viscosity at the exit is given by

$$\mu_e = \mu_0 \left(\frac{T_e}{T_0} \right)^{\frac{3}{2}} \frac{T_0 + S}{T_e + S}, \quad (72)$$

where $\mu_0 \simeq 1.716 \times 10^{-5}$ Pa s is the viscosity for air at the reference temperature, $T_0 \simeq 273.15$ K, and $S \simeq 110.4$ K is Sutherland's temperature. Hence, $\mu_e \simeq 1.7248 \times 10^{-5}$ Pa s with the density at the outlet being given by

$$\rho_e = \frac{Re\mu_e}{v_e c} \simeq 0.0687 \text{ kg m}^{-3}. \quad (73)$$

Finally, the pressure at the outlet and total pressure can be determined as

$$p_e = \rho_e R T_e \simeq 5419.3 \text{ Pa}, \quad (74)$$

$$p_i = p_e \left(1 + \frac{\gamma - 1}{2} M^2 \right)^{\frac{\gamma}{\gamma - 1}} \simeq 7198.5 \text{ Pa}, \quad (75)$$

which serve to fully specify the problem.

The linear T106c cascade used in the experiments of [Michlek et al. \(2012\)](#) consisted of six blades each with a span $h = 2.4c \simeq 0.22$ m. For the case under consideration the inlet turbulence was approximately 0.9%. To simplify the problem setup somewhat we will simulate just a single blade with a reduced span of $0.2c \simeq 0.0186$ m. The domain is periodic in the cross- and span-wise directions. On the surface of the blade an adiabatic wall condition is applied. A fixed total pressure condition is enforced on the inlet of the domain. This condition also enforces the desired pitch-wise angle for the incoming flow. At the exit a Riemann invariant boundary condition is applied. We note here that since Riemann invariant conditions are designed to minimise reflections at the boundary that they do not guarantee a strong enforcement of the exit pressure p_e . Hence, some tuning is required around the pressure enforced by the boundary condition in order to obtain the desired (averaged) exit pressure.

To mesh the domain unstructured hexahedral elements were employed. The elements on the boundary of the blade were quadratically curved and designed to fully resolved the near wall boundary layer region at $p = 2$. Specifically, the height of the first element was specified such that when $p = 2$ that the first solution point from the wall sits at $y+ \approx 1$ with

$$y+ = \frac{u_\tau \rho_e y}{\mu_e} = \frac{\sqrt{C_f} v_e \rho_e y}{\sqrt{2} \mu_e} \approx \frac{(2 \log_{10} Re - 0.65)^{-1.15} v_e \rho_e y}{\sqrt{2} \mu_e}, \quad (76)$$

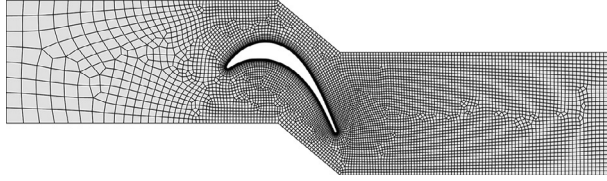


FIG. 13 Cutaway in the x - y plane of the unstructured hexahedral mesh used for the T106c test case. *Figure copyright F.D. Witherden and A. Jameson, reused with permission.*

where in the third step we have used the Schlichting skin friction formula to estimate C_f based off of the Reynolds number. The resulting mesh has a total of eight layers in the span-wise direction. In total the mesh contains 59,936 elements. A cut-away of the mesh can be seen in Fig. 13.

For the simulations a DG scheme was used for the spatial discretisation, a Rusanov Riemann solver was used to calculate the inviscid fluxes at element interfaces, and the explicit low-storage RK45[2R+] Runga–Kutta scheme of Kennedy et al. (2000) was used to advance the solution in time. Local temporal error was managed by utilising a PI type step size controller with absolute and relative error tolerances set to 10^{-5} . Solution points and flux points were placed at a tensor product construction of Gauss–Legendre quadrature points. The upwind and penalty parameters for the LDG scheme were set to $\beta = 1/2$ and $\tau = 1/10$, respectively. The Prandtl number was taken to be $Pr = 0.71$.

The simulations were run at $p = 1$ with a viscosity of $\mu = 3.4 \times 10^{-5}$ until $t = 2.5 \times 10^{-2}$. At this point the simulations were restarted with the correct viscosity of 1.7248×10^{-5} at order $p = 2$ and advanced to 3.5×10^{-2} . Time averaging of the pressure field was enabled at $t = 3.25 \times 10^{-2}$ with the average being accumulated every 50 time steps. This corresponds to approximately two passes over the chord.

A plot of isosurfaces of Q-criterion coloured by velocity magnitude for the fully developed flow are shown in Fig. 14. To compare with experimental data we consider the isentropic Mach number, defined as

$$M^{\text{isentropic}} = \sqrt{\frac{2}{\gamma - 1} \left(\left(\frac{p_e}{p} \right)^\Gamma - 1 \right)}, \quad (77)$$

where $\Gamma = (\gamma - 1)/\gamma$. A plot of the chord-wise distribution of this can be seen in Fig. 15. Looking at the figure also see that there is a strong level of agreement between PyFR and the experimental data of Michlek et al. (2012). However, there are some discrepancies around peak suction $x/c \sim 0.6$. We note however that such over-prediction has also been observed by both the studies of Hillewaert et al. (2014) and Garai et al. (2016).

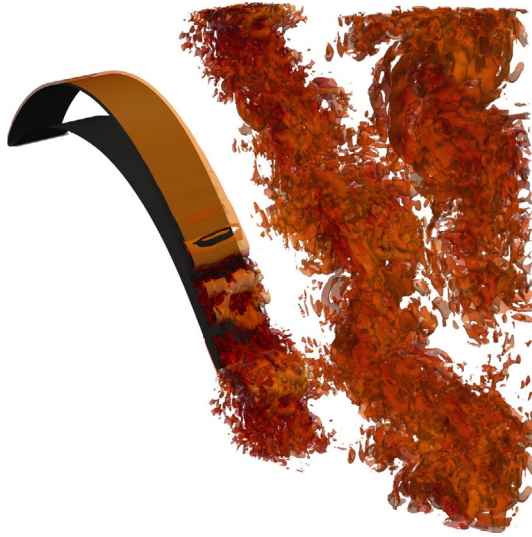


FIG. 14 Isosurfaces of Q-criterion coloured by velocity magnitude for the T106c test case with $p = 2$. Figure copyright F.D. Witherden and A. Jameson, reused with permission.

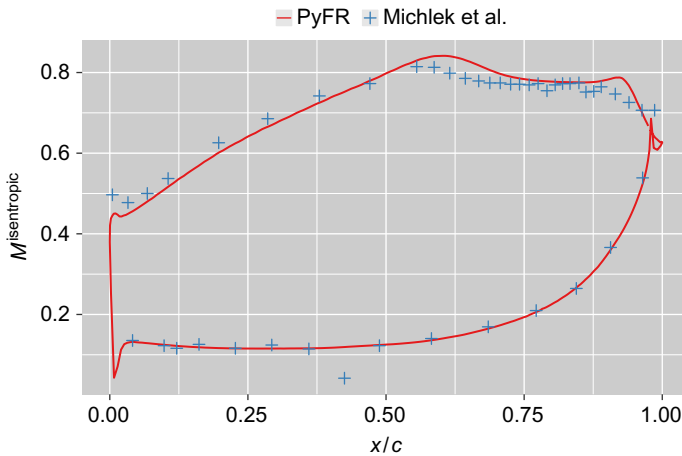


FIG. 15 Chord-wise distribution of the time- and span-averaged isentropic Mach number for the T106c test case compared against the experimental data of Michlek et al. (2012). Copyright F.D. Witherden and A. Jameson, reused with permission.

7 SUMMARY

This chapter has provided a review of the FR approach to the formulation of high-order methods that was first proposed by Huynh. This approach provides a unifying framework for the design of high-order discontinuous finite element methods for unstructured grids. As described in Section 2 the solution

in each element is represented by a polynomial u^D of degree p via a Lagrange type interpolating polynomial at $p + 1$ collocation points, typically the Gauss–Legendre points. A corresponding piecewise discontinuous flux polynomial f^D is similarly constructed via Lagrange interpolation. Interface fluxes at the element boundaries are computed based on an approximate Riemann solver from the left and right states at each interface, and a continuous flux f^C of degree $p + 1$ is then constructed by propagating the difference between the Riemann solution and the value of f^D into interior using correction polynomials of degree $p + 1$. The solution is then advanced by taking the divergence of the continuous flux f^C . The FR method can be extended to advection–diffusion problems by writing the equation as a first order system in a manner similar to DG methods.

The nature of a particular FR scheme to solve a hyperbolic conservation law depends on three factors: the location of the solution points, the choice of approximate Riemann solver for the interface fluxes, and the choice of the correction functions. It was shown by Huynh that the correction functions can be chosen to recover the nodal DG and spectral difference methods.

Section 4 outlines the ways in which the FR approach can be extended to multidimensional problems both for quadrilateral and hexahedral elements using a tensor product formulation, and to simplex elements by using vector correction functions restricted to lie in the Raviart–Thomas space of order p . The stability and accuracy of FR schemes is addressed in Section 5, highlighting in particular the form of energy stable FR schemes (proposed by Vincent et al., 2011b). Fourier analysis confirms that the expected order of accuracy is $p + 1$, but linear problems on uniform meshes with periodic boundary conditions can exhibit super-convergence.

Section 5 summarises the implementation aspects of FR schemes. The majority of operations can be cast in terms of matrix–matrix multiplications which can be deferred to special kernels. The open source PyFR software developed at Imperial College London by Witherden et al. (2014) exploits this to enable it to target a range of hardware platforms. Results obtained with PyFR confirm that when run at orders of four or more the FR method is particularly well suited to modern computing platforms on which arithmetic operations are very cheap, and memory fetches are relatively expensive. PyFR has exhibited performance at around 50% of machine peak in benchmark calculations on massively parallel GPU-based clusters.

Some applications to the Navier–Stokes equations are presented in Section 6. These indicate that at moderate Reynolds numbers the FR method can be used to perform accurate large eddy simulations without the introduction of a sub-grid model. This provides a path towards practical simulations of a variety of important industrial applications such as the design of the low-pressure turbine stages of jet engines.

REFERENCES

- Allaneau, Y., Jameson, A., 2011. Connections between the filtered discontinuous Galerkin method and the flux reconstruction approach to high order discretizations. *Comput. Methods Appl. Mech. Eng.* 200 (49), 3628–3636.
- Arnold, D.N., 1982. An interior penalty finite element method with discontinuous elements. *SIAM J. Numer. Anal.* 19 (4), 742–760.
- Asthana, K., Jameson, A., 2015. High-order flux reconstruction schemes with minimal dispersion and dissipation. *J. Sci. Comput.* 62 (3), 913–944.
- Asthana, K., Watkins, J., Jameson, A., 2016. *SIAM J. Numer. Anal.* (accepted for publication).
- Balan, A., May, G., Schöberl, J., 2011. A stable spectral difference method for triangles. In: 49th AIAA Aerospace Sciences Meeting including the New Horizons Forum and Aerospace Exposition, Aerospace Sciences Meetings.
- Bassi, F., Rebay, S., 1997. A high-order accurate discontinuous finite element method for the numerical solution of the compressible Navier-Stokes equations. *J. Comput. Phys.* 131 (2), 267–279.
- Bloor, M.S., 1964. The transition to turbulence in the wake of a circular cylinder. *J. Fluid Mech.* 19, 290–304.
- Breuer, M., 1998. Large eddy simulation of the subcritical flow past a circular cylinder. *Int. J. Numer. Methods Fluids* 28 (9), 1281–1302.
- Canuto, C., Hussaini, M.Y., Quarteroni, A., Zang, T.A., 2006. *Spectral Methods: Fundamentals in Single Domains*. Springer, Berlin.
- Castonguay, P., Vincent, P.E., Jameson, A., 2011. Application of high-order energy stable flux reconstruction schemes to the Euler equations. In: AIAA paper, 686.
- Castonguay, P., Vincent, P.E., Jameson, A., 2012. A new class of high-order energy stable flux reconstruction schemes for triangular elements. *J. Sci. Comput.* 51 (1), 224–256.
- Castonguay, P., Williams, D.M., Vincent, P.E., Jameson, A., 2013. Energy stable flux reconstruction schemes for advection-diffusion problems. *Comput. Methods Appl. Mech. Eng.* 267, 400–417.
- Cockburn, B., Shu, C.W., 1998. The local discontinuous Galerkin method for time-dependent convection-diffusion systems. *SIAM J. Numer. Anal.* 35 (6), 2440–2463.
- De Grazia, D., Mengaldo, G., Moxey, D., Vincent, P.E., Sherwin, S.J., 2014. Connections between the discontinuous Galerkin method and high-order flux reconstruction schemes. *Int. J. Numer. Methods Fluids* 75 (12), 860–877. <http://dx.doi.org/10.1002/fld.3915>.
- Gao, H., Wang, Z.J., 2009. A high-order lifting collocation penalty formulation for the Navier-Stokes equations on 2D mixed grids. In: 19th AIAA Computational Fluid Dynamics. San Antonio, TX.
- Garai, A., Diosady, L.T., Murman, S.M., Madavan, N., 2016. DNS of flow in a low-pressure turbine cascade with elevated inflow turbulence using a discontinuous-Galerkin spectral-element method. In: Proceedings of ASME Turbo Expo 2016.
- Gassner, G.J., 2013. A skew-symmetric discontinuous Galerkin spectral element discretization and its relation to SBP-SAT finite difference methods. *SIAM J. Sci. Comput.* 35 (3), A1233–A1253. <http://dx.doi.org/10.1137/120890144>.
- Harten, A., Engquist, B., Osher, S., Chakravarthy, S.R., 1987. Uniformly high order accurate essentially non-oscillatory schemes, III. *J. Comput. Phys.* 71 (2), 231–303.
- Hesthaven, J.S., Warburton, T., 2008. *Nodal Discontinuous Galerkin Methods: Algorithms, Analysis, and Applications*. vol. 54. Springer-Verlag, New York.

- Hillewaert, K., de Wiart, C.C., Verheylewegen, G., Arts, T., 2014. Assessment of a high-order discontinuous Galerkin method for the direct numerical simulation of transition at low-Reynolds number in the T106C high-lift low pressure turbine cascade. In: ASME Turbo Expo 2014: Turbine Technical Conference and Exposition. American Society of Mechanical Engineers, pp.V02BT39A034–V02BT39A034.
- Huynh, H.T., 2007. A flux reconstruction approach to high-order schemes including discontinuous Galerkin methods. In: 18th AIAA Computational Fluid Dynamics Conference, Fluid Dynamics and Co-located Conferences.
- Jameson, A., 2010. A proof of the stability of the spectral difference method for all orders of accuracy. *J. Sci. Comput.* 45 (1–3), 348–358.
- Jameson, A., Ou, K., 2011. 50 years of transonic aircraft design. *Prog. Aerosp. Sci.* 47 (5), 308–318.
- Jameson, A., Vincent, P.E., Castonguay, P., 2011. On the non-linear stability of flux reconstruction schemes. *J. Sci. Comput.* 50 (2), 434–445.
- Karniadakis, G., Sherwin, S.J., 2005. *Spectral/hp Element Methods for Computational Fluid Dynamics*. Oxford University Press, Oxford.
- Kennedy, C.A., Carpenter, M.H., Lewis, R.M., 2000. Low-storage, explicit Runge-Kutta schemes for the compressible Navier-Stokes equations. *Appl. Numer. Math.* 35 (3), 177–219.
- Kopriva, D.A., Koliias, J.H., 1996. A conservative staggered-grid Chebyshev multidomain method for compressible flows. *J. Comput. Phys.* 125 (1), 244–261.
- Kravchenko, A.G., Moin, P., 2000. Numerical studies of flow over a circular cylinder at $re_d = 3900$. *Phys. Fluids* 12, 403–417.
- Lehmkuhl, O., Rodriguez, I., Borrell, R., Oliva, A., 2013. Low-frequency unsteadiness in the vortex formation region of a circular cylinder. *Phys. Fluids* 25 (8), 3165–3168.
- Li, Y., Wang, Z.J., 2013. Evaluation of optimized CPR schemes for computational aeroacoustics benchmark problems. In: AIAA Paper 2013-2689.
- Liu, X.D., Osher, S., Chan, T., 1994. Weighted essentially non-oscillatory schemes. *J. Comput. Phys.* 115 (1), 200–212.
- Ma, X., Karamanos, G.S., Karniadakis, G.E., 2000. Dynamics and low-dimensionality of a turbulent near wake. *J. Fluid Mech.* 310, 29–65.
- Mengaldo, G., Grazia, D.D., Moxey, D., Vincent, P.E., Sherwin, S.J., 2015. Dealiasing techniques for high-order spectral element methods on regular and irregular grids. *J. Comput. Phys.* 299, 56–81. <http://dx.doi.org/10.1016/j.jcp.2015.06.032>.
- Mengaldo, G., De Grazia, D., Vincent, P.E., Sherwin, S.J., 2016. On the connections between discontinuous Galerkin and Flux Reconstruction schemes: extension to curvilinear meshes. *J. Sci. Comput.* 67 (3), 1272–1292. <http://dx.doi.org/10.1007/s10915-015-0119-z>.
- Michlek, J., Monaldi, M., Arts, T., 2012. Aerodynamic performance of a very high lift low pressure turbine airfoil (T106c) at low Reynolds and high mach number with effect of free stream turbulence intensity. *J. Turbomach.* 134 (6), 061009.
- Norberg, C., 1998. LDV measurements in the near wake of a circular cylinder. *Int. J. Numer. Methods Fluids* 28 (9), 1281–1302.
- Pacciani, R., Marconcini, M., Arnone, A., Bertini, F., 2011. An assessment of the laminar kinetic energy concept for the prediction of high-lift, low-Reynolds number cascade flows. *Proc. Inst. Mech. Eng. Part A: J. Power Energy* 225 (7), 995–1003.
- Park, J.S., Kim, C., 2016. Hierarchical multi-dimensional limiting strategy for correction procedure via reconstruction. *J. Comput. Phys.* 308, 57–80. <http://dx.doi.org/10.1016/j.jcp.2015.12.020>.

- Parnaudeau, P., Carlier, J., Heitz, D., Lamballais, E., 2008. Experimental and numerical studies of the flow over a circular cylinder at Reynolds number 3900. *Phys. Fluids* 20 (8), 085101.
- Peraire, J., Persson, P.O., 2008. The compact discontinuous Galerkin (CDG) method for elliptic problems. *SIAM J. Sci. Comput.* 30 (4), 1806–1824.
- Ranocha, H., Öffner, P., Sonar, T., 2016. Summation-by-parts operators for correction procedure via reconstruction. *J. Comput. Phys.* 311, 299–328. <http://dx.doi.org/10.1016/j.jcp.2016.02.009>.
- Raviart, P.A., Thomas, J.M., 1977. A mixed finite element method for 2-nd order elliptic problems. In: Galligani, I., Magenes, E. (Eds.), *Mathematical Aspects of Finite Element Methods*. Springer, Berlin, pp. 292–315.
- Reed, W.H., Hill, T.R., 1973. Triangular mesh methods for the neutron transport equation. Los Alamos Scientific Laboratory, Los Alamos. Technical Report LA-UR-73-479.
- Roe, P.L., 1981. Approximate Riemann solvers, parameter vectors, and difference schemes. *J. Comput. Phys.* 43 (2), 357–372.
- Roshko, A., 1953. On the development of turbulent wakes from vortex streets. California Institute of Technology. Technical Report NACA TR 1191.
- Sheshadri, A., Jameson, A., 2016. On the stability of the flux reconstruction schemes on quadrilateral elements for the linear advection equation. *J. Sci. Comput.* 67 (2), 769–790.
- Solin, P., Segeth, K., Dolezel, I., 2003. *Higher-Order Finite Element Methods*. CRC Press, Boca Raton, FL.
- Sun, Y., Wang, Z.J., Liu, Y., 2007. High-order multidomain spectral difference method for the Navier-Stokes equations on unstructured hexahedral grids. *Commun. Comput. Phys.* 2 (2), 310–333.
- Taylor, M.A., Wingate, B.A., Bos, L.P., 2005. Several new quadrature formulas for polynomial integration in the triangle. *Mathematics*. ArXiv:math/0501496.
- Uranga, A., Persson, P.O., Drela, M., Peraire, J., 2011. Implicit large eddy simulation of transition to turbulence at low Reynolds numbers using a discontinuous Galerkin method. *Int. J. Numer. Methods Eng.* 87 (1–5), 232–261.
- Vermeire, B.C., Nadarajah, S., 2013. Adaptive IMEX time-stepping for ILES using the correction procedure via reconstruction scheme. In: 21st AIAA Computational Fluid Dynamics Conference, Fluid Dynamics and Co-located Conferences.
- Vermeire, B.C., Nadarajah, S., 2015. Adaptive IMEX schemes for high-order unstructured methods. *J. Comput. Phys.* 280, 261–286.
- Vermeire, B.C., Cagnone, J.S., Nadarajah, S., 2013. ILES using the correction procedure via reconstruction scheme. In: 51st AIAA Aerospace Sciences Meeting including the New Horizons Forum and Aerospace Exposition, Aerospace Sciences Meetings.
- Vermeire, B.C., Nadarajah, S., Tucker, P.G., 2014. Canonical test cases for high-order unstructured implicit large Eddy simulation. In: 52nd Aerospace Sciences Meeting. AIAA SciTech.
- Vermeire, B.C., Nadarajah, S., Tucker, P.G., 2016. Implicit large eddy simulation using the high-order correction procedure via reconstruction scheme. *Int. J. Numer. Methods Fluids* 1097-0363. <http://dx.doi.org/10.1002/flid.4214>.
- Vincent, P.E., Jameson, A., 2011. Facilitating the adoption of unstructured high-order methods amongst a wider community of fluid dynamicists. *Math. Model. Nat. Phenom.* 6 (3), 97–140.
- Vincent, P.E., Castonguay, P., Jameson, A., 2011. Insights from von Neumann analysis of high-order flux reconstruction schemes. *J. Comput. Phys.* 230 (22), 8134–8154.
- Vincent, P.E., Castonguay, P., Jameson, A., 2011. A new class of high-order energy stable flux reconstruction schemes. *J. Sci. Comput.* 47 (1), 50–72.

- Vincent, P.E., Witherden, F.D., Farrington, A.M., Ntemos, G., Vermeire, B.C., Park, J.S., Iyer, A.S., 2015. PyFR: next-generation high-order computational fluid dynamics on many-core hardware. In: AIAA Paper 2015-3050.
- Wang, Z.J., Gao, H., 2009. A unifying lifting collocation penalty formulation including the discontinuous Galerkin, spectral volume/difference methods for conservation laws on mixed grids. *J. Comput. Phys.* 228 (21), 8161–8186.
- Williams, D.M., 2013. Energy stable high-order methods for simulating unsteady, viscous, compressible flows on unstructured grids (Ph.D. thesis). Stanford University.
- Williams, D.M., Jameson, A., 2013. Energy stable flux reconstruction schemes for advection-diffusion problems on tetrahedra. *J. Sci. Comput.* 59 (3), 721–7591.
- Williams, D.M., Castonguay, P., Vincent, P.E., Jameson, A., 2013. Energy stable flux reconstruction schemes for advection-diffusion problems on triangles. *J. Comput. Phys.* 250, 53–76.
- Williamson, C.H.K., 1988. The existence of two stages in the transition to three dimensionality of a cylinder wake. *Phys. Fluids* 31, 3165–3168.
- Williamson, C.H.K., 1996. Vortex dynamics in the cylinder wake. *Annu. Rev. Fluid Mech.* 28, 477–539.
- Witherden, F.D., Vincent, P.E., 2014. An analysis of solution point coordinates for flux reconstruction schemes on triangular elements. *J. Sci. Comput.* 61 (2), 398–423.
- Witherden, F.D., Farrington, A.M., Vincent, P.E., 2014. PyFR: an open source framework for solving advection-diffusion type problems on streaming architectures using the flux reconstruction approach. *Comput. Phys. Commun.* 185 (11), 3028–3040.
- Witherden, F.D., Vermeire, B.C., Vincent, P.E., 2015. Heterogeneous computing on mixed unstructured grids with PyFR. *Comput. Fluids* 120, 173–186.
- Witherden, F.D., Park, J.S., Vincent, P.E., 2016. An analysis of solution point coordinates for flux reconstruction schemes on tetrahedral elements. *J. Sci. Comput.* 69 (2), 905–920.
- Wood, J.R., Strasizar, T., Hathaway, M., 1990. Test Case E/CA-6, Subsonic Turbine Cascade T106. Test Cases for Computation of Internal Flows, AGARD-AR-275, July.
- Wozniak, B.D., Witherden, F.D., Russell, F.P., Vincent, P.E., Kelly, P.H.J., 2016. Gimmik generating bespoke matrix multiplication kernels for accelerators: application to high-order computational fluid dynamics. *Comput. Phys. Commun.* 202, 12–22.
- Yu, M., Wang, Z.J., 2013. On the connection between the correction and weighting functions in the correction procedure via reconstruction method. *J. Sci. Comput.* 54 (1), 227–244.